nature cell biology

ARTICLES

https://doi.org/10.1038/s41556-021-00654-5

Check for updates

Quantifying single-cell ERK dynamics in colorectal cancer organoids reveals EGFR as an amplifier of oncogenic MAPK pathway signalling

Bas Ponsioen[1,2], Jasmin B. Post[1,2], Julian R. Buissant des Amorie[1,2], Dimitrios Laskaris[1,2,10], Ravian L. van Ineveld[1,2,10], Simone Kersten[1,2,10], Andrea Bertotti[3,4], Francesco Sassi[3], François Sipieter[5,6,9], Benjamin Cappe[5,6], Sander Mertens[1,2], Ingrid Verlaan-Klink[1,2], Sylvia F. Boj[7], Rob G. J. Vries[7], Holger Rehmann[1], Peter Vandenabeele[5,6], Franck B. Riquet[5,6,8], Livio Trusolino[3,4], Johannes L. Bos[1,2] and Hugo J. G. Snippert[1,2] ✉

Direct targeting of the downstream mitogen-activated protein kinase (MAPK) pathway to suppress extracellular-regulated kinase (ERK) activation in *KRAS* and *BRAF* mutant colorectal cancer (CRC) has proven clinically unsuccessful, but promising results have been obtained with combination therapies including epidermal growth factor receptor (EGFR) inhibition. To elucidate the interplay between EGF signalling and ERK activation in tumours, we used patient-derived organoids (PDOs) from *KRAS* and *BRAF* mutant CRCs. PDOs resemble in vivo tumours, model treatment response and are compatible with live-cell microscopy. We established real-time, quantitative drug response assessment in PDOs with single-cell resolution, using our improved fluorescence resonance energy transfer (FRET)-based ERK biosensor EKAREN5. We show that oncogene-driven signalling is strikingly limited without EGFR activity and insufficient to sustain full proliferative potential. In PDOs and in vivo, upstream EGFR activity rigorously amplifies signal transduction efficiency in KRAS or BRAF mutant MAPK pathways. Our data provide a mechanistic understanding of the effectivity of EGFR inhibitors within combination therapies against *KRAS* and *BRAF* mutant CRC.

The mitogen-activated protein kinase (MAPK) pathway is among the most frequently deregulated signalling cascades in colorectal cancer (CRC), but effective therapeutic strategies to target *KRAS* or *BRAF* mutant CRC tumours have proven to be problematic[1,2]. Although oncogenic driver mutations prompt the constitutive activation of KRAS[3] and BRAF[4], most promising clinical results encompass inhibition of the MAPK pathway in combination with the upstream epidermal growth factor receptor (EGFR)[5–9]. The counterintuitive necessity to include upstream EGFR inhibition is often explained by the side effect of MAPK pathway inhibition, that is, the relief of extracellular-regulated kinase (ERK)-induced negative feedback, resulting in hyperactivated EGF receptors[10–12]. Conceptually, however, it is not entirely understood why downstream MAPK inhibition is incapable of intercepting these intensified EGFR signals. Furthermore, it raises the question to what extent mutant KRAS and BRAF activate downstream ERK in a fully autonomous fashion. Indeed, the notion that mutant KRAS acts fully independently of upstream signals has been challenged by genetic mouse models for lung and pancreatic cancer, where elimination of EGFR prohibited growth of KRAS mutant tumours[13–15].

ERK signalling responses in two-dimensional (2D) cell lines display a remarkable degree of cell-to-cell variability[16], such that time-course measurements at the population level overlook the dimension of cellular heterogeneity. Conversely, 'snapshot' approaches that collect single-cell data at fixed time points fail to capture dynamic behaviour, while ERK signalling is oscillatory in nature[16–19]. Monitoring single-cell ERK dynamics responding to pharmacological regimens in tumour tissue would greatly improve our understanding of responses to targeted therapies, for example by differentiating between scenarios of incomplete pathway suppression, cell-to-cell heterogeneities in drug response or subsequent ERK reactivation. However, ERK activity dynamics have not been studied with single-cell resolution in patient-derived tumour tissue.

Patient-derived organoids (PDOs) are robust 3D in vitro models that retain the histopathological features of in vivo tumours, including patient-specific drug responses[20–22]. Their scalability and reliability are of interest for the purposes of pre-clinical drug screenings, personalized medicine and drug development[20–25]. In particular, PDOs share the clinical relevance of patient-derived xenograft (PDX) models and constitute the most representative in vitro proxies of human tumours that are compatible with live-cell imaging of immediate cellular drug responses[26].

To understand the role of EGF signalling in *KRAS* and *BRAF* mutant CRC, we aimed to monitor ERK activities in CRC

[1]Molecular Cancer Research, Center for Molecular Medicine, University Medical Center Utrecht, Utrecht University, Utrecht, Netherlands. [2]Oncode Institute, Utrecht, Netherlands. [3]Laboratory of Translational Cancer Medicine, Candiolo Cancer Institute – FPO IRCCs, Candiolo, Torino, Italy. [4]Department of Oncology, University of Torino School of Medicine, Candiolo, Torino, Italy. [5]Molecular Signaling and Cell Death Unit, Department of Biomedical Molecular Biology, Ghent University, Ghent, Belgium. [6]Molecular Signaling and Cell Death Unit, Center for Inflammation Research (IRC), a VIB-UGent department, Ghent, Belgium. [7]Foundation Hubrecht Organoid Technology (HUB), Utrecht, Netherlands. [8]University of Lille, Villeneuve d'Ascq, France. [9]Present address: Institut Jacques Monod, CNRS UMR 7592, Université Paris Diderot, Paris, France. [10]These authors contributed equally: Dimitrios Laskaris, Ravian L. van Ineveld, Simone Kersten. ✉e-mail: h.j.g.snippert@umcutrecht.nl

organoids using a genetically encoded ERK biosensor. Although kinase translocation reporters (KTRs) are popular single-channel sensors[27], the compact, cell-dense architecture of PDOs argues against their use. In particular, robust quantification of nuclear shuttling is hampered by minimal cytoplasmic volumes in PDOs. By contrast, the FRET-based EKAREV biosensor[28] facilitates cell-specific readout in compact tissue thanks to its nuclear localization. EKAREV exploits the phosphorylation-dependent interaction between a CDC25C-derived sensor domain and a Pin1-derived ligand domain, thus translating ERK activity into changes in fluorescence resonance energy transfer (FRET). Because the sensor domain is also subject to specialized phosphatases, EKAREV eventually reports the kinase–phosphatase equilibrium as sensed by downstream targets of ERK, and it is exactly this equilibrium that orchestrates cellular responses. Moreover, investigations of transgenic mice indicate that EKAREV is compatible with cellular health[29].

In this Article, we apply FRET imaging in compact 3D PDOs to understand clinical drug responses. We re-engineered the EKAREV FRET sensor for ERK, generating so-called EKAREN5 (five enhancements). Most prominently, we resolved its undesired sensitivity to CDK1/cyclinB, increased its FRET range and broadened the detection range. Next, we established unbiased quantification of single-cell ERK activities over time. In CRC PDOs, we employed EKAREN5 to reveal ERK dynamics with single-cell precision and monitored their responses to targeted inhibition of EGFR and/or downstream nodes in the MAPK pathway.

Our work uncovers the critical importance of EGFR activity as an amplifier of intrinsically weak oncogenic KRAS and BRAF signalling to promote cellular proliferation.

Results

EKAREV modifications improve donor fluorophore, biosensor transgenesis and ERK specificity. To serve long-term applications in 3D PDOs, we first set out to replace the eCFP fluorescent protein of EKAREV[28] with the superior eCFP-variant Turquoise2 (Tq2)[30], which was designed to bear 169 silent mutations (Extended Data Fig. 4a) to minimize sequence homology[31]. As in EKAREV, we designed Tq2 to contain the dimerization-prone mutation K206A and we introduced V224L[32] to further enhance the affinity for YPet fluorescent protein. The resultant EKAREV(Tq) robustly registered ERK hyperactivation in HEK293 cells upon stimulation with phorbol-12-myristate-13-acetate (PMA), which activates RAF through PKC[33], and dynamically monitored spontaneous fluctuations in HeLa cells[16,17], establishing the unaffected reversibility of the sensor (Fig. 1a).

Second, EKAREV[28] may suffer undesired responsiveness to CDK1/cyclinB[17], as its ERK substrate sequence from CDC25C also serves as a consensus site for CDK1[34,35]. Indeed, HEK293 cells stably expressing EKAREV(Tq) showed ratio changes during mitosis that amounted to ~80–85% relative to PMA-induced saturation (Extended Data Fig. 1a–c and Supplementary Video 1), even in the presence of the MEK inhibitor selumetinib and ERK inhibitor SCH772984 (sel + SCH, both 5 μM) (Fig. 1b). Conversely, the CDK1 inhibitor RO-3363 induced substantial FRET loss in cells that were in M phase or G_2 phase (Extended Data Fig. 1e,f).

To resolve this undesired CDK1-sensitivity of EKAREV, we initially replaced its CDC25C-derived substrate sequence with alternative ERK substrate domains, anticipating that these may be refractory to CDK1 (Extended Data Fig. 4b). Although three of the seven tested substrates resulted in functional ERK biosensors, all variants retained undesired sensitivity to CDK1 (Extended Data Fig. 2a,b). Of note, ERK-KTR, which comprises an ELK1-derived sensor core, also shows gradual signal increase during G2 in HeLa cells (Fig. 1g). As for EKAREV(Tq), this rising slope predominantly reflects CDK1 activity (Extended Data Fig. 1g).

Next, we switched to targeting CDK1-sensitivity by re-engineering the CDC25C-derived substrate sequence in EKAREV(Tq). This sequence displays high homology to a substrate peptide used in crystallographic studies of the CDK2•cyclinA complex[36]. In this complex, the lysine at position +6 is deeply engaged in the interaction with cyclinA (Fig. 1c). This is specific for CDKs, as no cyclins are bound to ERK. To disrupt this interaction and disfavour phosphorylation by CDKs, we replaced this lysine with a bulky tryptophan (K426W). Furthermore, the lysine at position +4 was replaced by a proline (K424P), given that CDK1 favours basic residues C-terminal to the threonine[37], while ERK favours hydrophobic residues including prolines (www.phosphosite.org).

HEK293 cells stably expressing single-mutant EKAREV(Tq) variants revealed diminished levels of FRET during G2 and M phase relative to PMA-induced saturation (Fig. 1e). In particular, their combination substantially reduced the M-phase peak (from 80% to 11% of PMA-induced levels) and almost completely eliminated the rising slope during G2 phase (from 45% to 2%) (Fig. 1d,e′). Only RO-3306, and not sel+SCH, could further suppress EKAREV(PW) FRET in M-phase cells, indicating that its responsiveness to CDK1 during M phase is strongly reduced, but not fully eliminated. Attempts to further reduce CDK1 responsiveness with a third mutation (Extended Data Fig. 4c) were ineffective (Extended Data Fig. 2c). We will refer to EKAREV(PW) as EKAREN4. Finally, HeLa cells co-expressing ERK-KTR and EKAREN4 unambiguously

Fig. 1 | Minimizing cell-cycle-dependent influences on EKAREV(Tq)-FRET. a, Left: insertion of Turquoise2 cDNA, including 169 silent mutations (Extended Data Fig. 4a), into EKAREV. Middle: the FRET range of serum-starved HEK293 cells expressing parental EKAREV ($n = 55$ cells) versus EKAREV(Tq) ($n = 61$), approximated by PMA-induced sensor saturation (ΔR, %), remained unaffected (two independent experiments). Right: EKAREV(Tq) reports spontaneous fluctuations in HeLa cells. **b**, The typical mitotic EKAREV profile in HEK293 cells persists under selumetinib (MEKi) and SCH772984 (ERKi) (both 5 μM). Blue and yellow traces show Turq2 and YPet fluorescence intensities, respectively. Black: ratio of YPet/Turq2. Loss of fluorescence indicates nuclear envelope breakdown (NEB). c.k., cytokinesis. **c**, Top: crystal structure of the CDK2•cyclinA2 complex. CDK2 (yellow) and cyclinA2 (grey), shown as a space-filling model, and substrate peptide PK**T**PKKAKKL (orange) in ball-and-stick representation. The structure contains the transition state mimic ADP•AlF_3 resembling ATP (blue). Bottom: sequence comparison of substrate oligomer from the CDK2•cylcinA2 complex, CDK1 and ERK1 consensus, EKAREV sequence and the PW mutations. Red, threonine for phosphorylation; blue, mutated lysine (EKAREV(K424)); purple, mutated lysine that interacts with cyclinA2 (EKAREV(K426)); underlined, ERK-docking site. **d**, Representative trace of EKAREV(PW), alias 'PW', during G2 and M phase in HEK293 cells. **e**,**e′**, Quantification of M-phase peaks (**e**) and maximum FRET signal in late G2 (**e′**), measured in HEK293 cells stably expressing EKAREV or point mutant derivatives. Insets: values were normalized to PMA-induced sensor saturation. *P* values are calculated from the denoted cell numbers (*n*) (three independent experiments). **f**, Assessing the maximal FRET range (ΔR, %) of parental EKAREV(Tq), and mutant derivatives expressed at 'medium' levels. *P* values are calculated from the denoted cell numbers (*n*). **g**, Ratiometric traces for FRET and KTR output of monoclonal HeLa cells co-expressing EKAREV(Tq) and ERK-KTR-mCherry biosensors ($n = 25$ cells). Traces were synchronized on mitotic entry and are depicted as mean ratio ± s.d. *y*-axis ratios: FRET (YPF/CFP) and KTR (cytosol/nucleus). The arrow indicates mitotic entry. Scale bar, 10 μm. **h**, As in **g**, but for HeLa cells co-expressing EKAREN4 and ERK-KTR-mCherry. *P* values are calculated from $n = 26$ cells. Data are shown as mean ± s.d. Two-sided Student's *t*-tests: $^*P < 0.05$; $^{**}P < 0.001$; $^{***}P < 0.0005$. For all figures with box-and-whisker plots: boxes represent quartiles 2 and 3, the horizontal line represents the median and whiskers represent minimum and maximum within the 1.5× interquartile range. Dots are outliers.

illustrate that EKAREN4 is devoid of CDK1-sensitivity during G2 (Fig. 1h), eliminating all false-positive signals in morphologically indistinguishable G2 cells.

EKAREN4 displays an enhanced FRET range. Although the response kinetics of ERK activation (PMA) and subsequent inactivation (sel + SCH) were unaffected in EKAREN4 (Extended Data Fig. 2d), we noticed a beneficial ~1.5-fold enhanced ratio change upon saturating ERK activation (Fig. 1f). At extreme expression levels, the use of dimerization-prone fluorophores potentially creates a negative effect on FRET range by elevating baseline ratios, due to intermolecular FRET (Extended Data Fig. 2e,e′,f and Supplementary Discussion)[38]. Importantly, we verified that sensor kinetics remained unaffected despite >30-fold differences in expression levels (Extended Data Fig. 3d). Thus, to secure comparability within and across datasets, we measure FRET at standard-

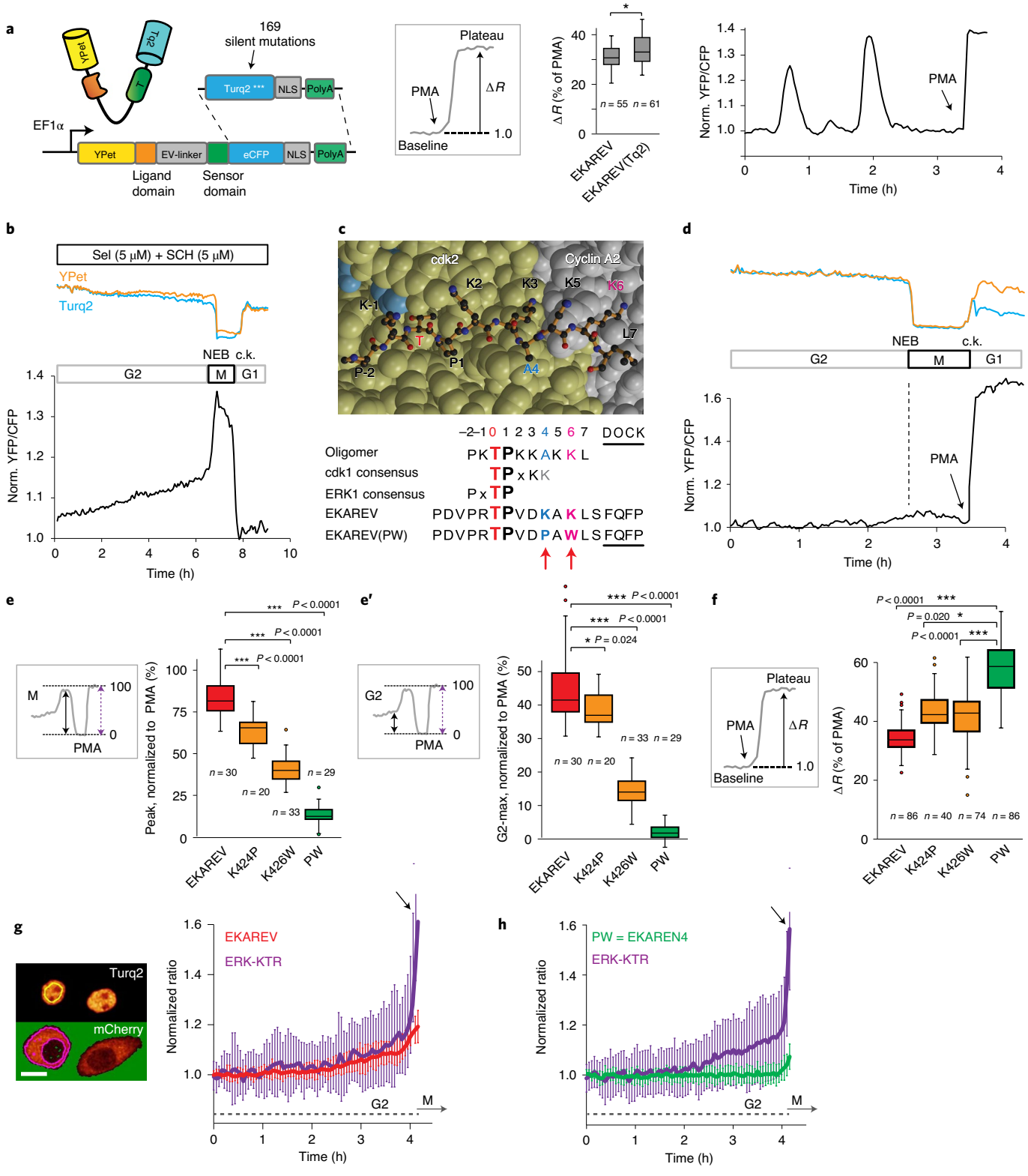

ized expression levels, preferably in the 'medium' range (Extended Data Fig. 2g).

EKAREN5 is the optimal FRET biosensor for measuring dynamic ERK activities. The detection range is defined as the window of activities that are dynamically and truthfully reported, from the lower detection limit (detection threshold) to the upper detection limit (saturation). Given that we aim for detailed examination of drug-induced ERK suppression in CRC PDOs, a low detection threshold is key. As a proxy for detection threshold, we determined the onset of EGF responses in serum-starved HeLa cells. To exclude variabilities in culture conditions or timing of stimulation, we co-cultured clonal HeLa-EKAREV(Tq) and HeLa-EKAREN4 cells and unmixed single-cell analyses in retrospect, based on response amplitude (Fig. 2a). Compared to EKAREV(Tq), EKAREN4 showed ~5.5-s delay in the time needed to exceed 5% ratio change (Fig. 2b), suggesting an increased detection threshold. Meanwhile, the saturation plateau was strongly delayed, indicating an extended detection range towards high ERK activities.

The detection threshold and saturation limit can be modulated by varying the linker length between sensor domain and ligand domain[28]. To correct the altered threshold of EKAREN4, we deleted 26 or 40 residues from the original linker (118 residues), generating linker length (LL) variants EKAREN4(LL92) and EKAREN4(LL78). Linker shortening resulted in faster onset times (Fig. 2b′,b′′), reflecting lowered detection thresholds. Linker shortening also lowered the upper detection limit. Still, EKAREN4(LL78) outperformed the parental EKAREV(Tq) at both extremes of the detection range. Furthermore, this variant, to which we will refer as EKAREN5, still displayed the beneficial characteristics previously documented for EKAREN4, that is (1) minimized ratio change during G2 and mitosis (Extended Data Fig. 2c), (2) enlarged FRET range (Extended Data Fig. 3a,b) and (3) unaltered dephosphorylation kinetics (Extended Data Fig. 3c).

We generated three clonal HeLa lines combining either EKAREV(Tq), EKAREN4 or EKAREN5 with ERK-KTR-mCherry, the latter serving as unbiased reference sensor to identify, quantify and subsequently cross-compare their detection of small physiological ERK activity fluctuations[39–41] (Supplementary Video 2), known to spontaneously occur in HeLa cells[16,17]. Generally, the relationship between KTR and FRET deviations remained proportional over a wide range of amplitudes (Fig. 2c,d), with EKAREV(Tq) displaying the steepest relationship.

'Small' ERK fluctuations (KTR ratio changes between 5% and 10%) were reliably detected by all three FRET sensor variants (Fig. 2e,f). However, 'very small' fluctuations (KTR changes <5%) were most accurately detected by EKAREV(Tq) and EKAREN5 (Fig. 2g), in agreement with the assessed detection thresholds (Fig. 2b). These outcomes were validated by various automated analyses on these double-sensor datasets (Extended Data Fig. 3e–h). Finally, we validated EKAREN5 performance by pairing FRET acquisition with conventional pERK immunostainings, showing a strong correlation at the single-cell level (r^2 of 0.87) (Extended Data Fig. 3i).

In conclusion, the name 'EKAREN' pays tribute to the parental variants EKAR[42] and EKAREV[28]. EKAREN5 (5x ENhanced) is the sensor of choice for general applications, in particular for detecting low (for example, drug-inhibited) ERK levels, while EKAREN4 suits studies on high ERK activities (Fig. 2h,i; see Supplementary Discussion for an elaborate discussion of biosensor characteristics).

Establishing quantitative single-cell readout of ERK dynamics in CRC PDOs using EKAREN5. PDOs recapitulate histopathological features of in vivo tumours and are compatible with live-cell microscopy, creating unique opportunities for the live readout of signalling activities at the cellular level. To examine the effects of targeted therapies against EGFR and/or the downstream MAPK pathway in KRAS and BRAF mutant CRCs, we stably introduced EKAREN5 into PDOs harbouring oncogenic MAPK pathways, that is, PDO-KRAS^{G12C}, PDO-KRAS^{G12V}, PDO-KRAS^{G12D}, PDO-NRAS^{Q61H} and PDO-BRAF^{V600E}(#1–4) as well as PDOs without mutations in the MAPK pathway, that is PDO-WT(#1) and PDO-WT(#2) (Supplementary Table 1).

To allow quantitative and comparative FRET analyses among these PDO lines, we systematically finalized time-lapse recordings with 'super-inhibition' of the pathway by combined application of MEK and ERK inhibitors (sel+SCH) and subsequent 'super-activation' with PMA and okadaic acid (OA), effectively assessing the minimal (0%) and maximal (100%) sensor output for each cell (Fig. 3a). Using this approach, normalized single-cell ERK activities can be interpreted free from arbitrary parameters that may affect absolute ratios, such as sensor expression level (Extended Data Fig. 2e), distance from the objective or depth within organoids (Extended Data Fig. 5). Furthermore, we developed a 'pick planes' tool to seamlessly follow 3D trajectories of individual cells of interest over time with optimal cross-sectioning of sensor-filled nuclei (Fig. 3a).

To demonstrate that we can monitor single-cell ERK activity levels during drug response, we treated PDO-KRAS^{G12V} with the clinical MEK inhibitor selumetinib[43]. Before treatment, virtually all cells showed extensive autonomous ERK fluctuations, similar to those observed in healthy mouse small intestinal organoids[18]. In response to selumetinib, cells showed immediate and near-complete ERK

Fig. 2 | Comparative analyses of EKAREV, EKAREN4 and EKAREN5. a, EGF responses of more than 100 co-seeded (1:1), serum-starved monoclonal HeLa cells expressing EKAREV or EKAREN4 (intervals of <2 s). Clustered response amplitudes of EKAREV and EKAREN4 allowed post-analysis unmixing. Dashed line: 5% threshold as a proxy for response onset time. Scale bar, 25 µm. The experiment was performed twice with identical results. **b**, As in **a**, comparing the response onset of parental EKAREV (red) versus EKAREN4 (green) linker length variants (numbers of amino acids are indicated). Shown are the averages of multiple single-cell analyses (*n* represents cells, indicated in the graphs) and zoomed-in rising phases. Response times are shown in corresponding colours: time to exceed 5% ratio change (dashed lines). The experiments in **b** and **b**′′ were performed twice. *n* represents cells, as indicated in the graphs. **c**, Fluctuations in HeLa cell are simultaneously detected by EKAREN5 and ERK-KTR-mCherry (representative example from $n > 100$). Insets: clonal HeLa cell expressing the nuclear FRET sensor and KTR biosensor. Scale bar, 10 µm. **d**, Scatter plot representing ERK fluctuations in low-density HeLa cells as their amplitudes in FRET and KTR signals. The r^2 values are taken from linear regression analyses. *n* represents analysed peaks, as indicated in the graph. **e**, Example of a small fluctuation in the KTR signal (purple), mirrored by EKAREN5 (blue) in high-density HeLa cells. Arrows indicate 5% KTR change and 0.5% FRET change. **f**, Matching scores (mean ratio ± s.d.) for co-detection of 'small' fluctuations (defined as 5–10% KTR ratio changes) with FRET biosensors, scrutinized from single-cell recordings (18 h). *P* values are calculated from *n* single-cell traces: EKAREV, 67 events/$n = 8$ traces; EKAREN4, 75 events/$n = 9$ traces; EKAREN5, 116 events/$n = 14$ traces. **g**, As in **f**. Co-detecting 'very small' fluctuations (defined as 0–5% KTR ratio changes), scrutinized from the same recordings. *P* values are calculated from *n* single-cell traces: EKAREV, 197 events/$n = 15$ traces; EKAREN4, 195 events/$n = 11$ traces; EKAREN5, 549 events/$n = 15$ traces. In **f** and **g**, two-sided Student's *t*-test was used: $^*P < 0.05$. NS, not significant. **h**, (1) EKAREV shows the steepest relationship (ERK activity versus FRET) and (2) the fastest sensor saturation. (3) EKAREN4 shows the latest sensor saturation towards high ERK. (4) EKAREN5 shows the lowest detection threshold (Det. thr.) with optimal detection range. EKAREN4/5 have enhanced dynamic FRET ranges. **i**, Overview of the biosensor characteristics. EKAREN5 is the sensor of choice, in particular at low (for example, drug-inhibited) ERK dynamics.

suppression at 1,000 nM, 200 nM and even 50 nM concentrations (Fig. 3b and Extended Data Fig. 6a–c). Underscoring the quantitative and sensitive nature of the procedure, we noticed few cells showing ERK reactivation within 2 h after start treatment (Extended Data Fig. 4d), substantially faster than previously reported ERK reactivation in selumetinib-treated 2D cell cultures[40]. With higher selumetinib concentrations, reactivation events declined in frequency and amplitude. Interestingly, ERK reactivation occurs heterogeneously, with marked differences even between neighbouring cells (Fig. 3b and Supplementary Video 3).

Next, we treated PDO-BRAF^{V600}(#3) with pan-RAF inhibitor LY3009120 and observed a similar heterogeneity in drug response, with a subset of cells showing rapid ERK reactivation[44]. Reminiscent of the reported interplay between MAPK inhibition and upstream EGFR activity[10,12], we could fully suppress reactivation by subsequent administration of the pan-HER inhibitor afatinib (Fig. 3c).

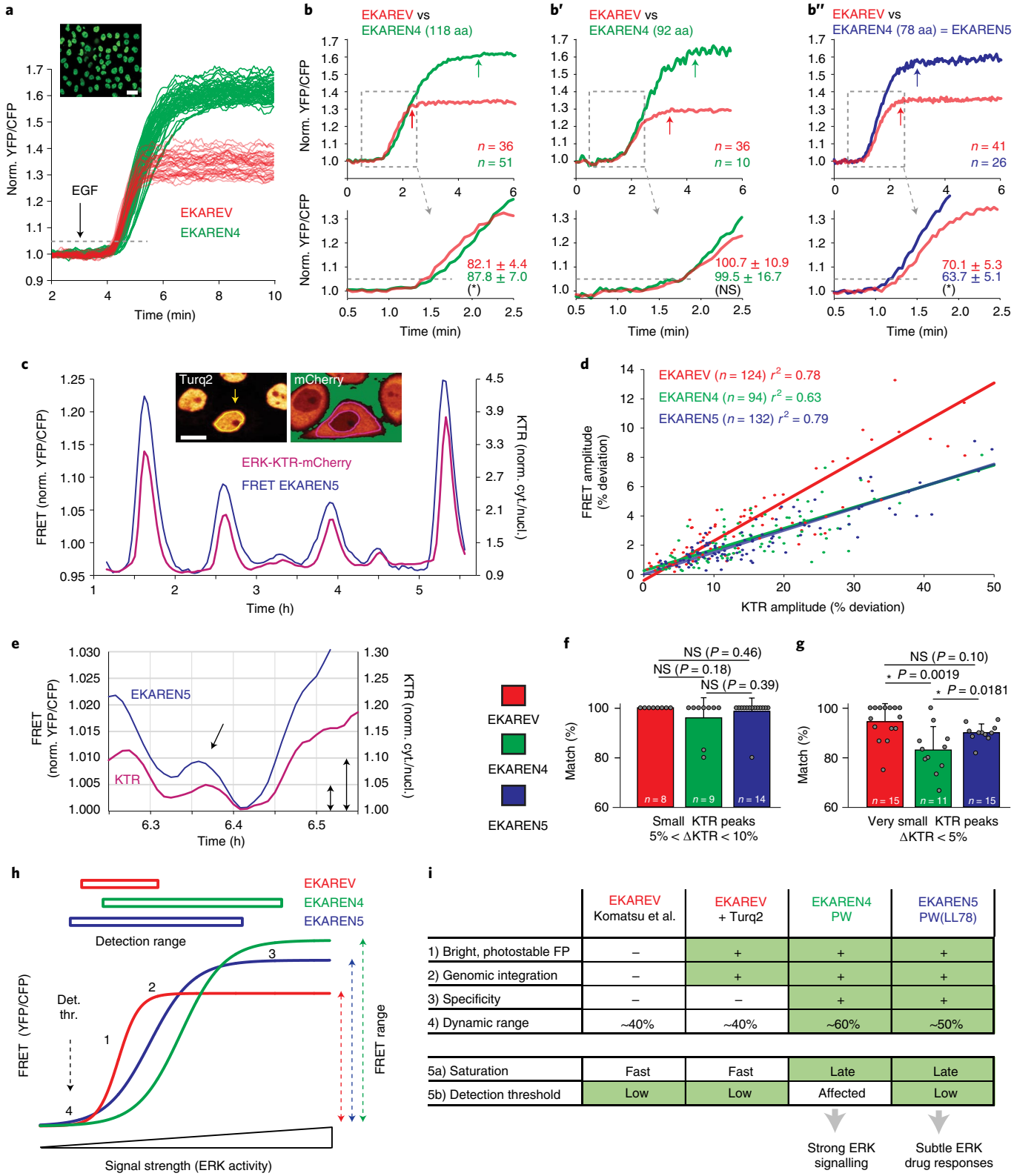

i

	EKAREV Komatsu et al.	EKAREV + Turq2	EKAREN4 PW	EKAREN5 PW(LL78)
1) Bright, photostable FP	–	+	+	+
2) Genomic integration	–	+	+	+
3) Specificity	–	–	+	+
4) Dynamic range	~40%	~40%	~60%	~50%
5a) Saturation	Fast	Fast	Late	Late
5b) Detection threshold	Low	Low	Affected	Low
			Strong ERK signalling	Subtle ERK drug responses

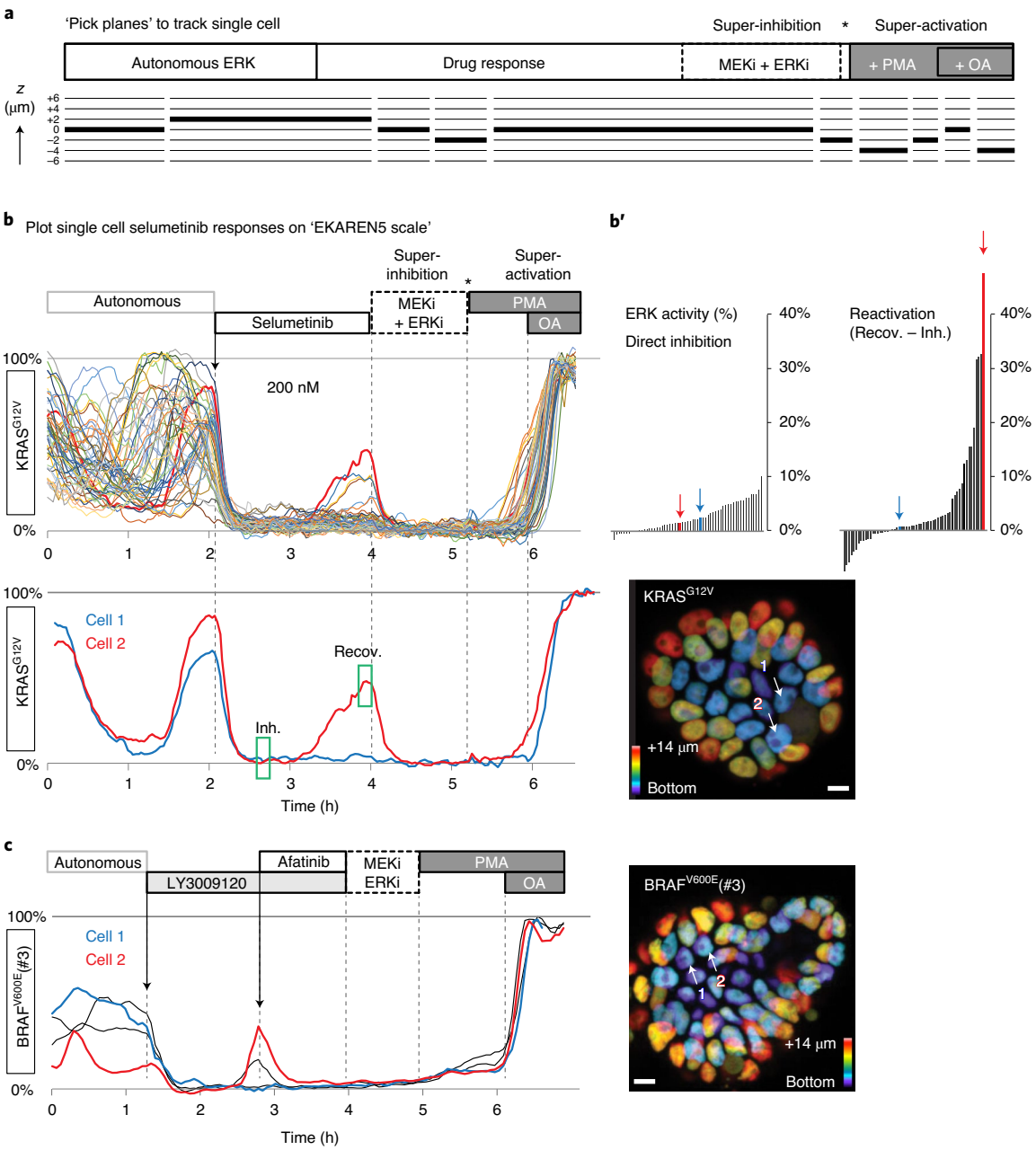

Fig. 3 | Single-cell ERK dynamics in CRC PDOs expose cell-to-cell heterogeneity in response to MAPK pathway inhibitors. a, CRC PDOs expressing the EKAREN5 ERK biosensor were imaged (*XYZT*) during 8–20 h with 2–4-min intervals. At the end of each experiment, minimum and maximum FRET signals were enforced by 'super-inhibition' (MEK-inh selumetinib (5 µM) and ERK-inh SCH772984 (5 µM)) and subsequent 'super-activation' (PMA (150 nM) and subsequent okadaic acid (OA, 1 µM)). Inhibitors were washed out before super-activation (asterisk). For bona fide analysis of single cells moving in 3D, we developed a tool to 'pick planes', ensuring that the resulting two-dimensional (2D; *XYT*) excerpts seamlessly follow the trajectories of individual cells of interest over time, with optimal cross-sectioning of the sensor-filled nuclei (Methods). **b**, Top: single-cell ERK responses to the MEK inhibitor selumetinib (200 nM, approximating clinical plasma concentrations[43]) in EKAREN5-expressing PDO-KRAS^{G12V}, imaged and analysed as outlined in **a**. Shown are single-cell responses from 59 cells in three simultaneously imaged PDOs. Bottom: example responses of two neighbouring cells displaying distinct recovery from ERK inhibition over the course of 2 h. The corresponding cell 1 and cell 2 are indicated in the depth-coded organoid image. See also Supplementary Video 3. The experiment was performed twice. **b′**, Waterfall plots summarizing the direct inhibition effect of selumetinib (green box, 'Inh', in **b**) and the recovery effect (difference between green box 'Inh.' and green box 'Recov.', in **b**). Coloured bars (indicated by arrows) represent cell 1 and cell 2. **c**, PDO-BRAF^{V600E}(#3) organoids were subjected to pan-HER inhibitor LY3009120 (1 µM). Most cells showed full inhibition (blue), but a subset of cells (red) showed rapid ERK reactivation, sensitive to afatinib (1 µM). Scale bars, 10 µm. The experiment was performed once.

pan-HER inhibitor afatinib eliminates ERK activity oscillations in PDOs mutant for KRAS, NRAS or BRAF. Niche factor-independent tumour growth is progressively associated with the adenoma–carcinoma transition in CRC[24]. Oncogenic KRAS mutations are generally assumed to render tumour cells independent of growth factor EGF. However, this contradicts the defining role for EGFR in KRAS mutant lung[13] and pancreatic[14,15] tumorigenesis. To better understand the interplay between EGFR and

downstream MAPK pathway mutations, we monitored ERK activity dynamics upon inhibition of upstream EGFR in PDO-KRAS^{G12V}. Despite the presence of downstream mutant KRAS, fluctuating ERK activity was instantly and substantially suppressed by afatinib treatment (Fig. 4a), even at 50 nM (Extended Data Fig. 7a). The alternative pan-HER inhibitors lapatinib and dacometinib, as well as the EGFR-specific inhibitors gefitinib, erlotinib and cetuximab antibody, similarly inhibited oscillatory ERK activity, while the HER2-specific inhibitor CP-724714 did not (Extended Data Fig. 7b–d).

Afatinib-induced elimination of oscillatory ERK activity was also observed in PDO-KRAS^{G12C}, PDO-KRAS^{G12D} and PDO-NRAS^{Q61H} (Fig. 4a), as well as in the PDO-BRAF^{V600E}(#1), (#2) and (#3) (Fig. 4b and Supplementary Video 4) and PDO-WT(#1) and (#2) (Fig. 4c). These data indicate that EGFR remains a major driver of ERK activity in tumour cells of human CRCs, despite oncogenic mutations in *KRAS* or *BRAF*.

Of note, residual ERK activity levels, becoming apparent upon afatinib-induced elimination of upstream signalling input, were of minor level, devoid of oscillatory behaviour and probably reflect constitutive oncogenic signalling by mutant RAS or RAF (Fig. 4a,b). Indeed, such residual ERK activity was not observed in PDO-WT(#1) or (#2) (Fig. 4c). Interestingly, PDO-BRAF^{V600E}(#4), the only PDO without obvious ERK activity oscillations, appeared refractory to afatinib treatment (Fig. 4b′′), suggesting that its high ERK levels arise independent of EGFR signalling. Inhibition of the adaptor protein Shp2 (SHP099, 5 µM), which couples a broad range of receptor tyrosine kinases (RTKs) to downstream RAS, was also without effect, as were inhibitors for Src, FAK, cKit or PDGF (Extended Data Fig. 7f,f′). Thus, MAPK activity in PDO-BRAF^{V600E}(#4), as an exception in our PDO panel, is independent of upstream input.

In agreement with previous data underpinning the central role of EGFR in orchestrating ERK oscillations in 2D cell lines[39], our single-cell derivations from CRC PDOs display instant deflections when afatinib is administered during the rising phase of an ERK activity oscillation (for example, Extended Data Fig. 7e), further establishing EGFR as the critical driver of ERK oscillations. We confirmed the effects of afatinib using western blot analysis, showing near-absent pERK levels in PDO-WT(#1), while afatinib could substantially reduce, but not eliminate, the pERK signal in mutant PDOs (Fig. 4e).

Next, we aimed to identify the signalling components responsible for the EGFR-driven ERK activity oscillations and EGFR-independent residual ERK levels. The latter probably follows from constitutive oncogenic signalling, given the mutational status of the examined CRC organoids. In line with this assumption, EGFR-independent oncogenic signalling was completely suppressed by pan-RAF inhibitor LY3009120, lowering FRET ratios to levels indiscernible from those enforced by MAPK pathway super-inhibition (Fig. 4d). These data indicate that neither of the signalling inputs feeding into ERK involves pathways circumventing the RAF-module. To test that EGFR activity establishes ERK oscillations via the linear RAS–RAF–MEK cascade, we enabled doxycyclin-induced overexpression[45] of HRAS^{N17}, which impedes signalling of all RAS isoforms through dominant-negative sequestering of upstream guanine nucleotide exchange factors (GEFs)[46]. HRAS^{N17}-induced cells, marked by nuclear mKate2-NLS (Extended Data Fig. 7g), failed to generate ERK activity oscillations, but showed minor levels of steady-state ERK activity that were insensitive to afatinib (Fig. 4f). Taken together, EGFR drives ERK activity oscillations via the linear RAS-MAPK pathway (Fig. 4g). These observations are in accordance with integral biochemical analyses on EGFR-MAPK-pathway components (Extended Data Fig. 7h).

We next wondered whether EGFR signalling engages mutant MAPK signalling components themselves. AMG-510, a drug that specifically targets the cysteine of KRAS^{G12C} (ref. [47]), substantially reduced ERK activity in PDO-KRAS^{G12C} (>50%; Fig. 5a), which is at odds with the limited intrinsic activity of KRAS^{G12C} (few %) in situations without upstream signalling input. Moreover, the sustained pulsatile dynamics of the residual ERK activity indicates ongoing EGFR-mediated signalling through the non-inhibited wild-type RAS isoforms (Fig. 5a–c). Finally, expression of EKAREN5 in RASless MEFs, in which reconstituted KRAS mutants (G12C, G12D, G12V or G13D) replace all deleted endogenous RAS isoforms[48], revealed substantially boosted ERK activity upon EGF stimulation (Fig. 5d). Although mutant KRAS isoforms established higher basal ERK levels (Fig. 5d′), their signal transduction effectivity is enhanced upon EGFR activation, similar to their wild-type counterparts.

Differential adaptation to long-term growth conditions without EGF. Given the substantial contribution of EGFR-mediated oscillations to total ERK activity, we wondered to what extent this is controlled by the external supply of EGF ligands via culture conditions. We therefore derived PDO sister lines through long-term culturing (8–13 weeks) under either minimal (200× diluted) or zero EGF (Fig. 6a). All *RAS*-mutant PDOs appeared largely unchanged in their autonomous pulsatile ERK profiles, with only a mild reduction

Fig. 4 | Pan-HER inhibitor afatinib eliminates ERK activity oscillations in KRAS, NRAS or BRAF mutant PDOs. a,**b**, EKAREN5 reveals ERK activity in CRC PDOs before and after afatinib administration (200 nM). Shown are YFP/CFP ratios, normalized to levels at super-inhibition (0%) and super-activation (100%). After afatinib-induced ERK suppression, basal ERK level is revealed by further FRET decrease upon super-inhibition (arrow). Unlike other PDOs, BRAF^{V600E}(#4) does not respond to afatinib. Dashed traces show *z*-plane analyses comprising multiple cells. The solid line shows a representative single-cell analysis from the corresponding *z*-plane. BRAF^{V600E}(#3) (blue) results are also shown in Supplementary Video 4. **c**, As in **a**, the drug responses to afatinib (200 nM) in PDO-WT(#1) and (#2). Unlike RAS/BRAF mutant PDOs, afatinib-induced ERK suppression leaves no residual basal levels (dashed circle). Characteristically, dynamics in WT PDOs showed either high-amplitude fluctuations (black) or relatively constant dynamics (grey). **d**, Following afatinib treatment, pan-RAF inhibitor LY3009120 (1 µM) abolishes basal ERK activity in KRAS mutant (top) and BRAF mutant (bottom) PDOs (dashed circle; no further reduction upon super-inhibition). Shown are *z*-plane analyses. **e**, Western blot analyses on the indicated PDO lines recapitulate the above-described EKAREN5 observations. In particular, afatinib abolished pERK in PDO-WT(#1), while in mutant PDOs pERK was largely affected, but not abolished. Afatinib, 200 nM; super-inhibition, sel + SCH, 5 µM; super-activation, PMA + OA. SE, short exposure; LE, long exposure. Vinculin was used as loading control. The experiment was performed twice. Blots for PDO-WT(#1) and PDO-KRAS^{G12C} were from the experiment also depicted in Extended Data Fig. 7h. **e′**, Quantification of the western blots in **e**. The pERK signal was normalized to the vinculin signal (relative to maximal induction, PMA + OA). **f**, Doxycyclin-inducible expression of mKate2-NLS-P2A-HRAS^{N17} (top) was established in PDO-KRAS^{G12C}, PDO-NRAS^{Q61H} and PDO-BRAF^{V600E}(#3) via lentiviral infection. FRET acquisition after 20 h of doxycyclin incubation. Analysis on HRAS^{N17}-positive cells (marked by mKate2-NLS) reveals loss of oscillatory ERK behaviour. Super-inhibition (arrow), but not afatinib, could further suppress basal ERK levels. Traces are single-cell analyses. Inset: mKate2-NLS (red) merged with EKAREN5 (green) in BRAF^{V600E}(#3) organoid. The blue trace is derived from the cell indicated by the blue arrow. Scale bar, 10 µm. The experiment was performed once. **g**, EGFR employs the linear MAPK pathway to induce pulsatile ERK activation, involving both wild-type and mutant KRAS. **g′**, Model depicting ERK activity patterns in *KRAS*^{G12X} or *BRAF*^{V600E} mutant PDOs as composites of basal 'oncogenic' signalling and EGFR-mediated ERK activity oscillations.

in overall ERK phosphorylation status in PDOs cultured without EGF (Fig. 6d). Pulsatile ERK dynamics were similarly sensitive to afatinib (Fig. 6b), suggesting that these PDOs established autocrine and/or paracrine EGFR stimulation. Of note, in PDO-KRAS^{G12V} and PDO-NRAS^{Q61H}, these challenging growth conditions provoked adaptive enhancement of ERK activation by oncogenic RAS (Fig. 6′), hinting either at direct signalling rewiring or at clonal selection over the course of weeks.

Unlike the *RAS* mutants, EGF-deprived PDO-BRAF^{V600E}(#1) and (#2) appeared less inclined to restore EGF signalling. Compared to their EGF-stimulated parental lines, they showed loss of pulsatile dynamics (Fig. 6c), reduction in mean ERK activity levels and no impact of afatinib treatment (Fig. 6c′). Interestingly, PDO-BRAF^{V600E}(#3), which displayed the lowest basal ERK level among the BRAF^{V600E}-mutant PDOs (Fig. 4), was the only one to restore its high-amplitude ERK oscillations, but these were now largely insensitive to afatinib (Fig. 6c,c′), suggesting that an alternative signal replaced EGFR to maintain ERK oscillations.

Thus, most CRC PDOs maintain oscillatory ERK activity patterns despite limiting EGF conditions, possibly through the

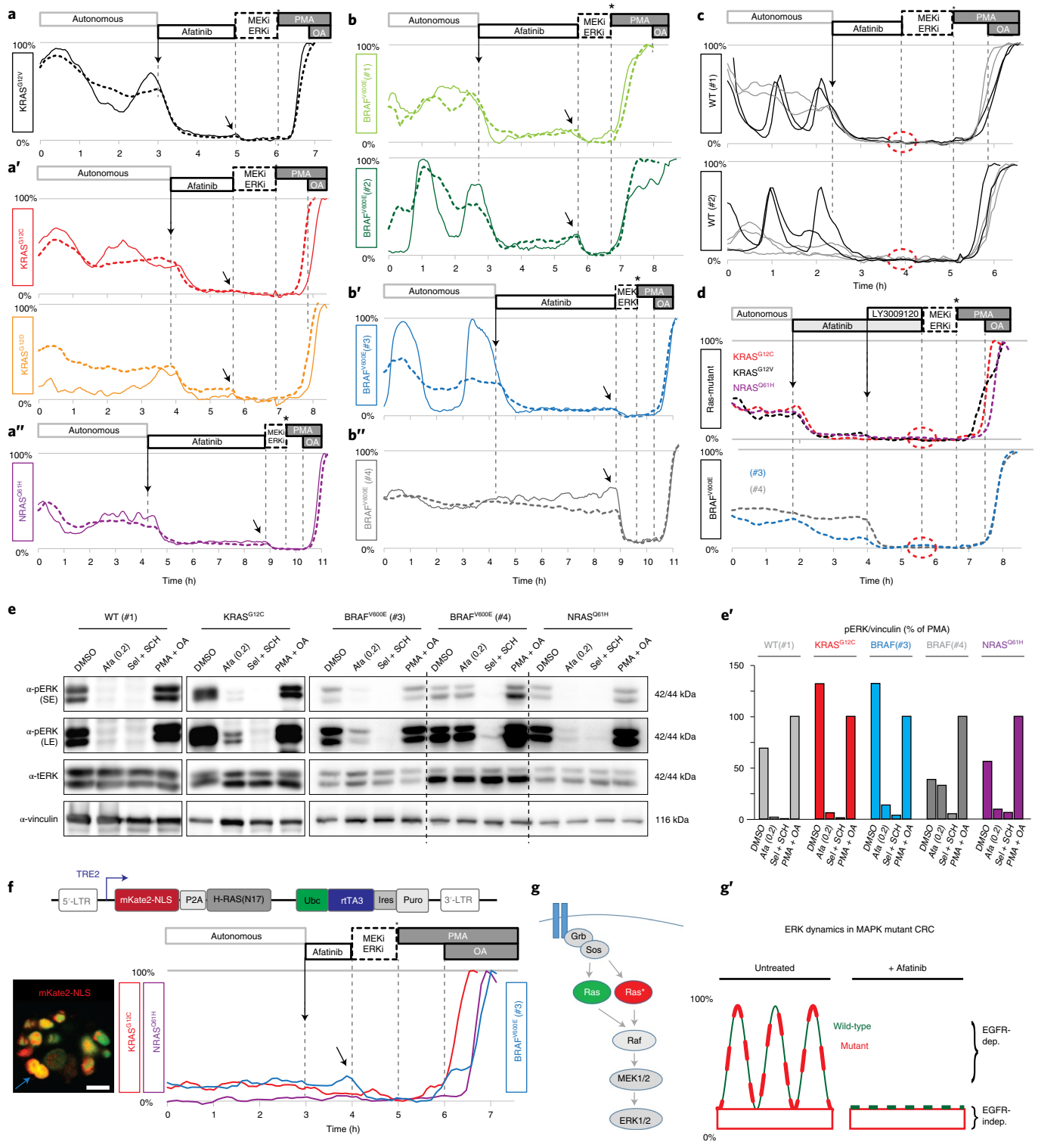

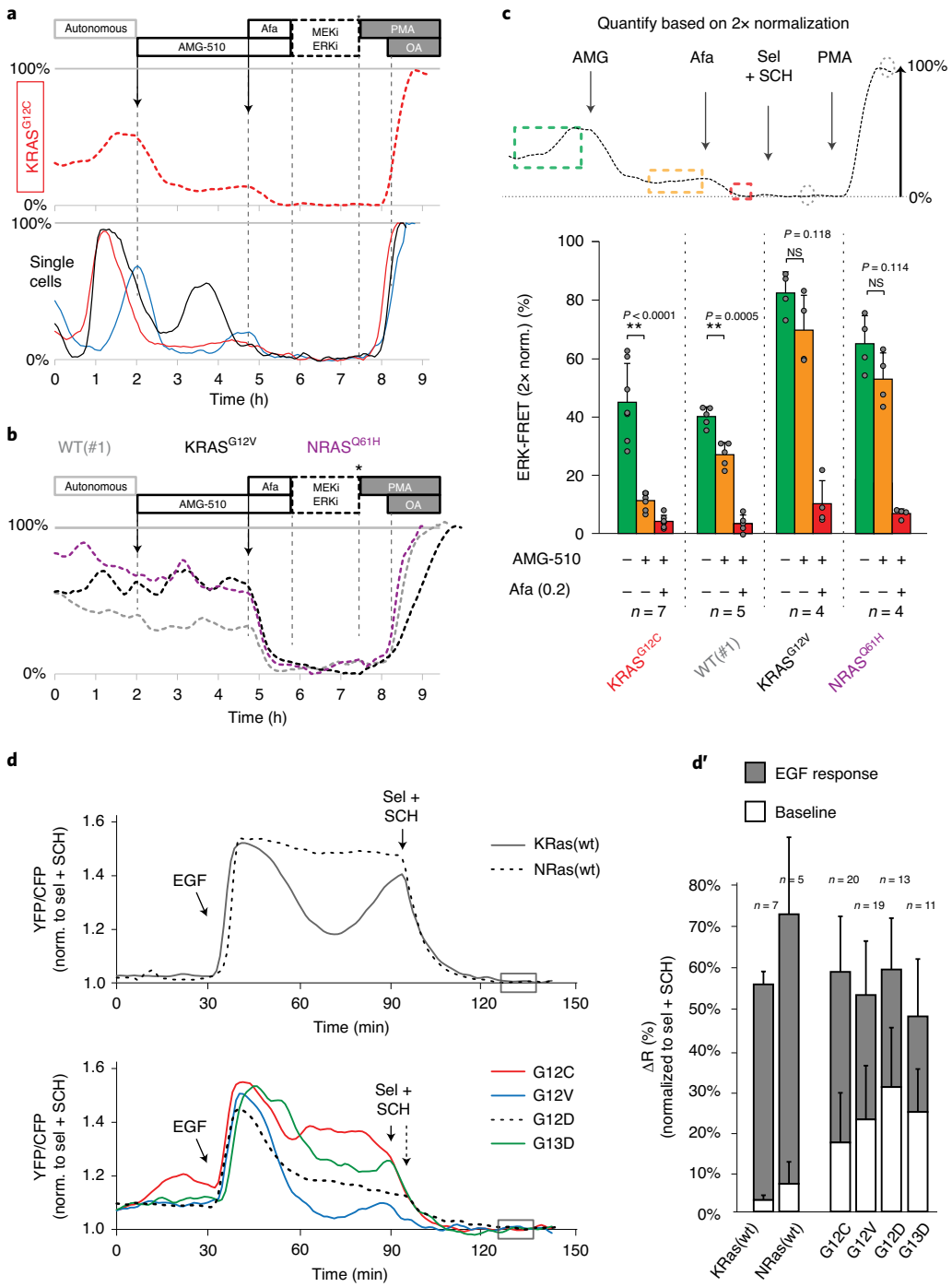

Fig. 5 | Mutant KRAS molecules engage in EGFR-mediated ERK activation. a, KRAS^{G12C} was specifically targeted by AMG-510 (250 nM) in PDO-KRAS^{G12C}, inducing substantial suppression of ERK activity. Top: plane analysis. Bottom: single cells from the same organoid. Unlike in afatinib responses (for example, Fig. 4a), residual ERK activity remains characterized by pulsatile dynamics (of various amplitude), probably representing EGFR activity relayed by the unhindered wild-type RAS proteins. **b**, Three CRC PDOs containing either wild-type or different RAS mutants were scanned in parallel, excluding non-specific effects of AMG-510 (250 nM) on ERK signalling. Plane analyses are shown. **c**, Top: scheme for the analysis of EKAREN5 dynamics before and after drug administration on a double calibrated scale. Bottom: bar graph summarizing PDO responses before (green), to AMG-510 (orange) and to AMG-510 + afatinib (200 nM; red). Data are presented as mean values ± s.d. *n* numbers represent individual PDOs (individual data points) and are stated in the graph for each group. Representative traces are shown in **a** and **b**. The experiment was performed twice. Two-sided Student's *t*-test: $^*P < 0.05$. NS, not significant. **d**, EKAREN5 was introduced into RASless MEFs harbouring RAS reconstitutions, being wild-type (top) or one of four mutants (bottom). The MEF sister lines were serum-starved 24 h before EGF stimulation, clearly indicating amplified signal transduction by mutant RAS upon EGFR activity. The FRET signal is normalized to super-inhibition (box). **d′**, Quantification of all single-cell analyses. *n* numbers indicate cells and are denoted in the graph for each group. Data are presented as mean values ± s.d.

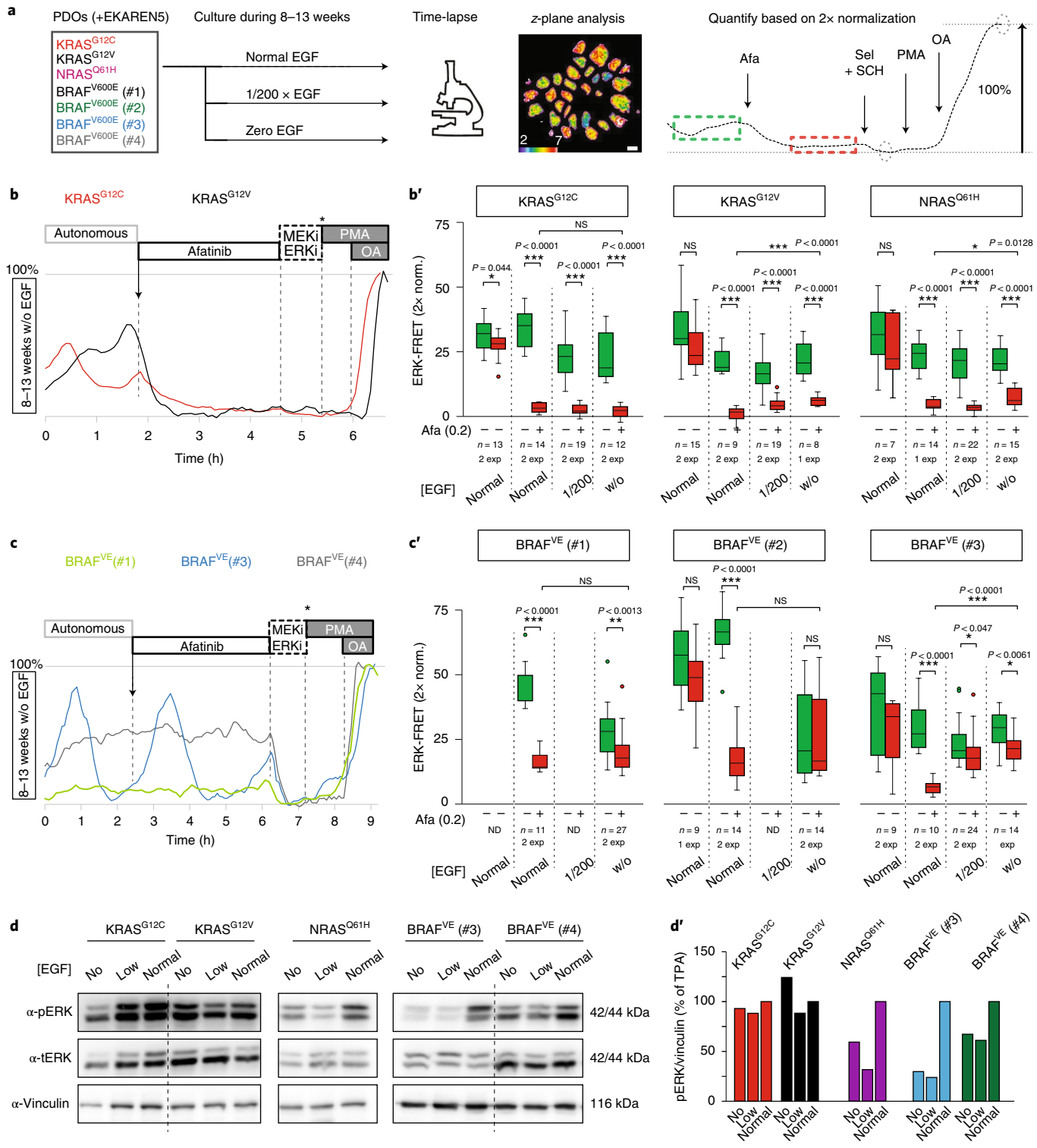

production of growth factors that activate EGFR or other ERK-coupled RTKs.

EGFR-mediated amplification of ERK signalling promotes tumour growth in vitro and in vivo. We set out to assign functional importance to oncogene-mediated basal signalling versus additional signal amplification by upstream EGFR, with regard to survival and/or proliferation of tumour cells. For this, we studied the long-term effects of EGFR inhibition on *KRAS*^{G12X} and *BRAF*^{V600E} mutant organoids. First, we confirmed sustained ERK suppression by afatinib over long intervals (20 h, Fig. 7a). After three or eight days of incubation, we also observed similarly low basal ERK levels, devoid of EGFR-driven oscillatory amplification (Fig. 7b and Extended Data Fig. 7a,b). Intriguingly, long-term inhibition of these continuous oscillatory dynamics unmasked a hidden pattern of extremely rare, isolated spikes in few cells (incidence, one per ~30 h; Extended Data Fig. 7b), indicative of alternative signalling input.

Next, we scored organoid growth in conditions with or without EGFR-induced signal amplification. PDO-KRAS^{G12C} showed

Fig. 6 | Differential adaptation to long-term growth conditions without EGF. a, Culturing scheme to assess the role of EGF supplementation to the PDO culture medium. PDOs were cultured in medium containing standard EGF (50 ng ml^{-1}), 200× diluted EGF (0.25 ng ml^{-1}) or no EGF. After 8–13 weeks, PDOs were FRET-imaged during afatinib treatment (200 nM) and *z*-plane analysis was performed (the example FRET image shows the region of interest defined in purple). Right: example trace (representative for $n > 10$). Green dashed box, mean ERK before treatment; red dashed box, mean ERK after treatment. Afatinib-induced ERK suppression was quantified according to double calibration (circles, ERK_{min} and ERK_{max}). Scale bar, 10 µm. **b**, After 8–13 weeks of culturing without EGF supplementation, the persistent ERK activity oscillations in PDO-KRAS^{G12C} (red) and PDO-KRAS^{G12V} (black) showed sensitivity to afatinib. Shown are representative single-cell analyses. **b′**, Effects of pan-HER inhibition on ERK activity levels, quantification as outlined in **a**. Green, before afatinib; red, after mock or afatinib (200 nM) inhibition. Indicated are PDO numbers (*n*), pooled from one or two experiments (exp). **c**, As in **b**, single-cell ERK traces from three PDO-*BRAF*^{V600E} mutant PDOs cultured without EGF. ERK dynamics in BRAF^{V600E}(#1) are now without oscillations. Although BRAF^{V600E}(#3) (blue) still shows oscillatory ERK dynamics, the majority of cells have become unresponsive to afatinib. BRAF^{V600E}(#4) (grey) remains insensitive to afatinib. **c′**, Effects of pan-HER inhibition on ERK activity levels, with quantification as outlined in **a**. Green, before afatinib; red, after mock or afatinib (200 nM) inhibition. PDO numbers (*n*) are indicated. The experiment was performed at least twice (each comprising 10–25 organoids). ND, not done. In **b′** and **c′**, boxes represent quartiles 2 and 3, the horizontal line represents the median and the whiskers represent minimum and maximum within 1.5× interquartile range. Dots are outliers. Two-sided Student's *t*-tests: $*P < 0.05$; $**P < 0.005$; $***P < 0.0005$. NS, not significant. **d**, Western blot analysis of ERK activity status in PDO lines. 'Low', 200× reduced EGF (0.25 ng ml^{-1}) supplementation. 'No', without EGF supplementation. Vinculin was used as a loading control. Left: *RAS* mutant PDO lines; right, *BRAF*^{V600E} mutant PDO lines. The experiment was performed once. **d′**, Quantification of the results in **d**.

near-complete growth suppression under afatinib treatment, but limited cell death, as assessed by growth recovery after drug release (Fig. 7c). These observations suggest that the minimal signalling from oncogenic KRAS^{G12C} (Fig. 6b′) suffices to maintain cell survival, while signal amplification by EGFR promotes proliferation. Interestingly, combining afatinib with pan-RAF inhibitor LY3009120, which eliminates residual oncogene-driven ERK activity (Fig. 4d), induced increased mortality in PDO-KRAS^{G12C}.

By contrast, in PDO-KRAS^{G12V}, PDO-NRAS^{Q61H} and PDO-BRAF^{V600E}(#3), afatinib alone could reduce but not stop proliferation. However, the combination of afatinib and LY3009120 halted proliferation in all PDO lines (Fig. 7c,d). As expected, this drug combination induced substantial mortality in PDO-BRAF^{V600E}(#3), while the growth-arrested PDO-KRAS^{G12V} and PDO-NRAS^{Q61H} showed signs of survival. Differential effects on viability in the absence of any ERK activity may result from additional cancer mutations, such as the oncogenic *PIK3CA* mutation in PDO-KRAS^{G12V} (ref. [49]). Of note, LY3009120 alone could not halt proliferation, underscoring that effective inhibition of oncogenic MAPK signalling benefits from silenced EGFR signalling. Also when applying the clinically applied EGFR/RAF/MEK triple combination for BRAF mutant CRC[7], we observed optimal growth suppression and ERK inactivation when downstream RAF + MEK inhibition (encorafinib + binimetinib) was complemented with upstream EGFR inhibition (cetuximab) (Extended Data Fig. 9).

To validate the impact of upstream EGFR activity on oncogenic MAPK signalling in vivo, we analysed the biochemical and therapeutic effects of EGFR blockade using a series of CRC PDX models with mutant KRAS or BRAF that had been annotated for response to the clinically approved anti-EGFR antibody cetuximab in an independent study[50] (Fig. 7e). Although we have not shown oscillatory signalling in vivo[18,51], we do here confirm reduced pERK levels upon cetuximab treatment in all models examined (9/9) (Fig. 7f,g). Analogous to clinical observations, the response to cetuximab of most of these models was originally categorized as progressive disease[50]. Nevertheless, closer examination of tumour growth data between cetuximab-treated and placebo-treated animals illustrated that reduced pERK levels in tumours were frequently accompanied by reduced growth kinetics (~40% over all 10 PDX models, Fig. 7h). Thus, also in vivo, EGFR activity amplifies the downstream signalling activity of an oncogenic MAPK pathway.

Discussion

To understand drug responses in human tumours with mutated MAPK pathways, we captured the dynamic nature of single-cell ERK profiles in CRC PDOs. For this, we re-engineered the pre-existing ERK biosensor into EKAREN5. The enhancements relate to specificity, FRET range, detection range, fluorophore properties and genomic integration (see Supplementary Discussion for extensive discussion of EKAREN5 and FRET measurements in 3D organoids). Subsequently, our standardized double-normalization procedure proved essential for quantitative analyses to reveal cell-to-cell variabilities and low-amplitude ERK levels in the response to clinical inhibitors.

Fig. 7 | EGFR-mediated amplification of ERK signalling promotes tumour growth in vitro and in vivo. a, Representative FRET traces (*z*-plane analyses) of EKAREN5 post afatinib treatment in KRAS^{G12C}, BRAF^{V600E}(#2) and BRAF^{V600E}(#3) show the sustained absence of EGFR-mediated amplification. **b**, As in **a**, but with FRET imaging initiated 72 h post afatinib treatment. Basal ERK levels remain unaltered during the long-term drug response. **c**, Monitoring organoid growth of five-day-old PDO-KRAS^{G12C} during eight days of drug treatment, followed by five days without drugs to test growth re-initiation of viable organoids (asterisks indicate medium refreshments). Drug concentrations (µM) are indicated. Representative brightfield images were taken at days 5, 13 and 18. Right: EKAREN5 YPet fluorescence was used for object segmentation for size measurement (~103 PDOs per data point), as depicted in the corresponding graphs (mean ± s.e.m.). The experiment was performed twice. Scale bar, 50 µm. #, unreliable measurement (overgrowth) of 18-day-old DMSO-treated PDOs. **d**, As in **c**. The graphs depict the mean organoid size (±s.e.m.) during drug treatment on KRAS^{G12V}, NRAS^{Q61H} and BRAF^{V600E}(#3) PDOs. The experiment was performed twice. The mean numbers of objects (PDOs) per time point are KRAS^{G12V}, 59; NRAS^{Q61H}, 84; BRAF^{V600E}(#3), 107. The exact *n* numbers per presented data point in **c** and **d** are provided in the source data. **e**–**h**, Frozen sections were taken from experiments performed for Bertotti and colleagues[50]. **e**, Schematic of PDX model generation from metastatic CRC samples[50] for prospective examination of cetuximab response. **f**, Changes in pERK levels were scored through immunohistochemistry on paraffin-embedded tumour sections after two weeks of cetuximab or placebo treatment in three independent mice bearing PDX from the same tumour. Shown are representative sections from KRAS^{G12D}-mutant PDX model M245, showing a strong reduction in pERK levels following cetuximab treatment. Scale bar, 100 µm. **g**, Graph depicting quantified changes in pERK levels for 9 out of 10 PDX models of CRC (oncogenic mutations are indicated). Changes in pERK levels were scored through immunohistochemistry as the average of 10 optical fields (×40), randomly chosen from each tumour ($n = 30$). A minimum of two mice per group were analysed. **h**, Comparative re-analysis of tumour growth data per PDX model upon treatment with cetuximab ($n = 6$ mice) or placebo (six mice)[50]. Top: bar graph representing tumour size variation from baseline of untreated and cetuximab-treated animals. Bottom: bar graph representing tumour growth inhibition (%, treated/untreated) calculated from size variation.

In the current study, we reveal extensive ERK activity oscillations in CRC PDOs with either wild-type or mutant MAPK signalling (for example, *KRAS*^{G12X}, *NRAS*^{Q61H} or *BRAF*^{V600E}). These oscillatory dynamics were eliminated by pan-HER as well as more EGFR-specific inhibitors, confirming the central role of EGFR[18,39]. Upon EGFR inhibition, we observed surprisingly low levels of basal, non-oscillatory ERK activity remaining, which we attribute to the intrinsic activity of oncogenic KRAS^{G12X}, NRAS^{Q61H} or BRAF^{V600E}. Thus, ERK patterns are composites of limited basal signalling from oncogenes plus a much larger EGFR-driven pulsatile component. Importantly, even without EGF supplementation, all RAS mutants showed EGFR-induced oscillations, probably explained

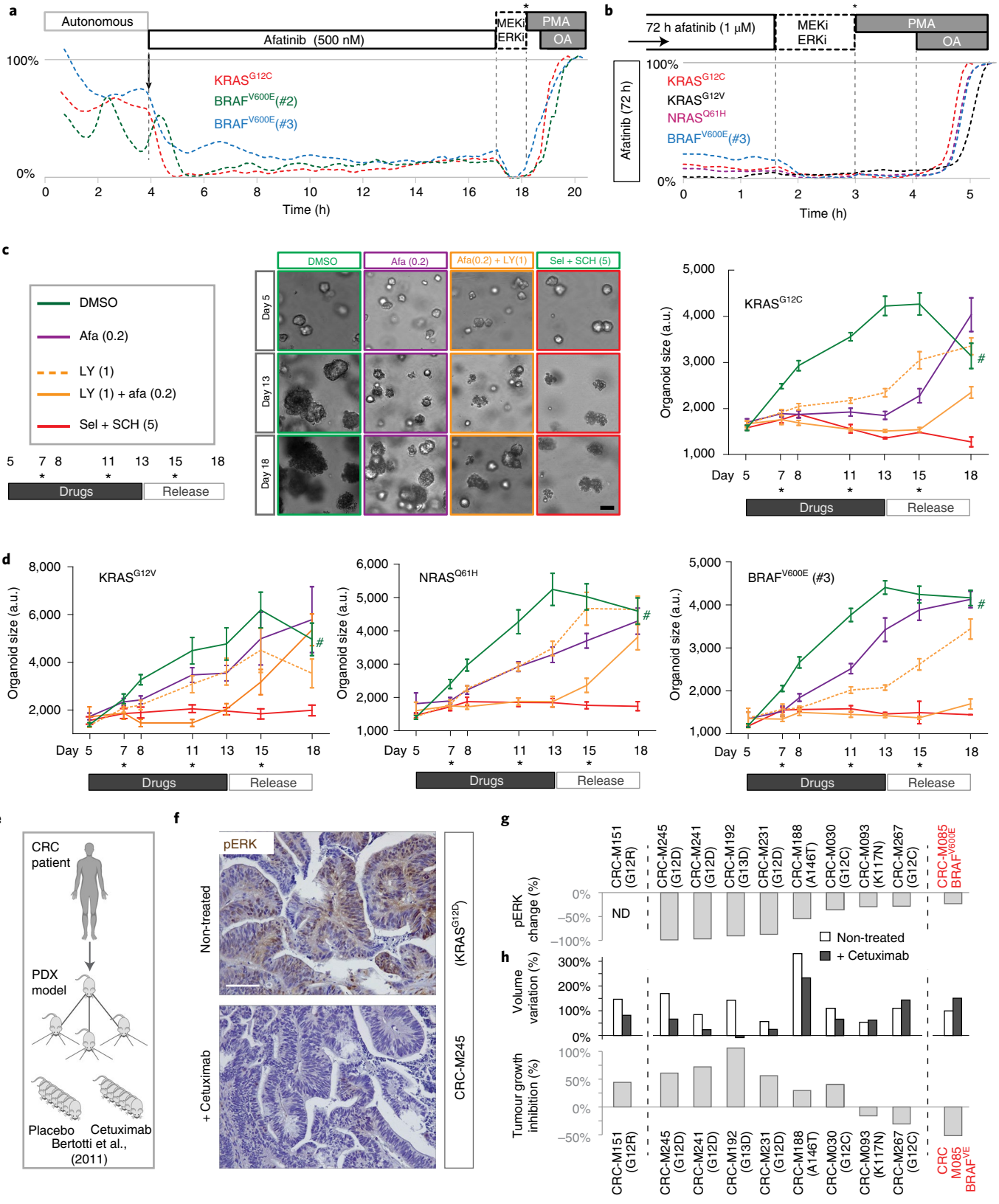

by autonomous production of EGF(-like) ligands establishing autocrine/paracrine signalling. Unlike the RAS mutants, PDO-BRAF^{V600E}(#3) re-established ERK oscillations through an EGFR-independent mechanism, while PDOs BRAF^{V600E}(#1) and (#2) showed no signs of evolutionary pressure to elevate their already substantial basal ERK activity.

EGFR-driven ERK activity oscillations employ the linear MAPK pathway, given that they disappear upon overexpression of d.n.HRAS^{N17} or incubation with pan-RAF inhibitor. In physiological MAPK signalling, EGFR functions as a switch by initiating a cascade of events, including activation of RAS-GEFs, clustering of activated RAS, recruitment and dimerization of RAF and subsequent assembly of the RAS–RAF–MEK complex with scaffold KSR (kinase suppressor of Ras)[52]. These events catalyse signalling efficiency by local enrichment of the involved signalling molecules. Based on our quantitative assessments, KRAS^{G12X}, NRAS^{Q61H} and BRAF^{V600E} possess limited intrinsic signalling activity[3,4], but with EGFR activated, their transduction efficiency is maximized, presumably by such complex formation. Indeed, it has been reported that the activity of mutant KRAS can benefit from upstream GEF activity[53–57]. This notion is substantiated by our observations in RASless MEFs harbouring reconstituted RAS mutants and in our *KRAS*^{G12C} organoids, in which ERK activity was substantially impacted by the G12C-specific drug AMG-510. BRAF^{V600E}, well known for its capacity to signal independently as a monomer, is also expected to benefit from upstream signals, as it can heterodimerize with wild-type CRAF under the influence of active RAS[4,58].

In line with the essential role of ERK unveiled in mouse tumour models[59], complete elimination of ERK activity through co-inhibition of MEK and ERK successfully induced cytotoxicity in all studied PDOs. pan-HER inhibition reduced growth kinetics in all mutant lines, albeit to variable degrees. Most notably, minimal basal ERK levels, as in PDO-KRAS^{G12C}, suffice to survive treatment. Overall, fundamental fate decisions towards apoptosis, survival or proliferation seem to be driven by minimal differences in ERK activity levels in the lower range of the spectrum (from 0–5 to >10%, resp.).

Upon long-term EGF deprivation, RAS-mutant PDOs maintained oscillatory ERK activity via autonomous production of EGF(-like) ligands, exemplifying the concept that EGF-independent tumour growth is not automatically secured with the sole presence of RAS oncogenes. Paracrine or microenvironment-derived EGFR stimuli can provide essential amplification of oncogenic MAPK signalling to promote tumour growth, as we also deduced from multiple PDX models of CRC cancer (Fig. 7). Accordingly, transcriptome analysis of human CRCs identified increased levels of paracrine EGFR stimuli in tumour tissue[60]. Autocrine production of EGFR-activating ligands has been demonstrated to predict the response to EGFR inhibition[61–63].

Importantly, in all studied PDOs, combined pan-HER and pan-RAF inhibition successfully imposed growth arrest, as opposed to single treatments. This also accounted for complementing MEK+RAF inhibition with cetuximab in *BRAF*^{V600E} mutants, in analogy to recent clinical evaluations[7]. The fact that ERK inactivation by MAPK pathway inhibitors benefits instantly from silenced EGFR activity underscores the clinical relevance of EGFR as a major amplifier of oncogenic MAPK signalling. This mechanistic insight is in accordance with the recently reported efficacy of G12C inhibitor AMG-510 when combined with cetuximab[8]. On a similar note, EGFR activity was shown to be a prerequisite for KRAS-driven tumorigenesis of pancreatic ductal adenocarcinoma[14,15] and non-small-cell lung cancer[13].

Most pharmacological strategies to treat KRAS or BRAF mutant CRC patients involve 'vertical targeting' of multiple MAPK effectors including upstream EGFR[5,7], the feedback activation of which became a known resistance mechanism following downstream MAPK pathway inhibition[8,10–12]. Our data provide mechanistic significance to this notion by revealing that EGFR signalling actively amplifies the signalling output of oncogenic MAPK effectors.

Suppressing this amplification by pharmacological targeting of EGFR is an indispensable component of combinatorial treatments against MAPK mutant CRC.

Online content

Any methods, additional references, Nature Research reporting summaries, source data, extended data, supplementary information, acknowledgements, peer review information; details of author contributions and competing interests; and statements of data and code availability are available at https://doi.org/10.1038/s41556-021-00654-5.

Received: 21 February 2020; Accepted: 24 February 2021;
Published online: 1 April 2021

References

1. Ryan, M. B. & Corcoran, R. B. Therapeutic strategies to target *RAS*-mutant cancers. *Nat. Rev. Clin. Oncol.* **15**, 709–720 (2018).
2. Yaeger, R. & Corcoran, R. B. Targeting alterations in the RAF-MEK pathway. *Cancer Discov.* **9**, 329–341 (2019).
3. Karnoub, A. E. & Weinberg, R. A. Ras oncogenes: split personalities. *Nat. Rev. Mol. Cell Biol.* **9**, 517–531 (2008).
4. Yao, Z. et al. BRAF mutants evade ERK-dependent feedback by different mechanisms that determine their sensitivity to pharmacologic inhibition. *Cancer Cell* **28**, 370–383 (2015).
5. Corcoran, R. B. et al. Combined BRAF, EGFR and MEK inhibition in patients with *BRAF*^{V600E}-mutant colorectal cancer. *Cancer Discov.* **8**, 428–443 (2018).
6. van Geel, R. et al. A phase Ib dose-escalation study of encorafenib and cetuximab with or without alpelisib in metastatic *BRAF*-mutant colorectal cancer. *Cancer Discov.* **7**, 610–619 (2017).
7. Kopetz, S. et al. Encorafenib, binimetinib and cetuximab in *BRAF* V600E-mutated colorectal cancer. *New Engl. J. Med.* **381**, 1632–1643 (2019).
8. Amodio, V. et al. EGFR blockade reverts resistance to KRAS(G12C) inhibition in colorectal cancer. *Cancer Discov.* **10**, 1129–1139 (2020).
9. Huijberts, S. et al. Phase I study of lapatinib plus trametinib in patients with *KRAS*-mutant colorectal, non-small cell lung and pancreatic cancer. *Cancer Chemother. Pharmacol.* **85**, 917–930 (2020).
10. Prahallad, A. et al. Unresponsiveness of colon cancer to BRAF(V600E) inhibition through feedback activation of EGFR. *Nature* **483**, 100–103 (2012).
11. Sun, C. et al. Intrinsic resistance to MEK inhibition in *KRAS* mutant lung and colon cancer through transcriptional induction of ERBB3. *Cell Rep.* **7**, 86–93 (2014).
12. Corcoran, R. B. et al. EGFR-mediated re-activation of MAPK signaling contributes to insensitivity of *BRAF* mutant colorectal cancers to RAF inhibition with vemurafenib. *Cancer Discov.* **2**, 227–235 (2012).
13. Moll, H. P. et al. Afatinib restrains K-RAS-driven lung tumorigenesis. *Sci. Transl. Med.* **10**, eaao2301 (2018).
14. Ardito, C. M. et al. EGF receptor is required for KRAS-induced pancreatic tumorigenesis. *Cancer Cell* **22**, 304–317 (2012).
15. Navas, C. et al. EGF receptor signaling is essential for K-*RAS* oncogene-driven pancreatic ductal adenocarcinoma. *Cancer Cell* **22**, 318–330 (2012).
16. Albeck, J. G., Mills, G. B. & Brugge, J. S. Frequency-modulated pulses of ERK activity transmit quantitative proliferation signals. *Mol. Cell* **49**, 249–261 (2013).
17. Aoki, K. et al. Stochastic ERK activation induced by noise and cell-to-cell propagation regulates cell density-dependent proliferation. *Mol. Cell* **52**, 529–540 (2013).
18. Muta, Y. et al. Composite regulation of ERK activity dynamics underlying tumour-specific traits in the intestine. *Nat. Commun.* **9**, 2174 (2018).
19. Bugaj, L. J. et al. Cancer mutations and targeted drugs can disrupt dynamic signal encoding by the Ras-Erk pathway. *Science* **361**, eaao3048 (2018).
20. Vlachogiannis, G. et al. Patient-derived organoids model treatment response of metastatic gastrointestinal cancers. *Science* **359**, 920–926 (2018).
21. Ganesh, K. et al. A rectal cancer organoid platform to study individual responses to chemoradiation. *Nat. Med.* **25**, 1607–1614 (2019).
22. Yao, Y. et al. Patient-derived organoids predict chemoradiation responses of locally advanced rectal cancer. *Cell Stem Cell* **26**, 17–26 (2020).
23. van de Wetering, M. et al. Prospective derivation of a living organoid biobank of colorectal cancer patients. *Cell* **161**, 933–945 (2015).
24. Fujii, M. et al. A colorectal tumor organoid library demonstrates progressive loss of niche factor requirements during tumorigenesis. *Cell Stem Cell* **18**, 827–838 (2016).

25. Pauli, C. et al. Personalized in vitro and in vivo cancer models to guide precision medicine. *Cancer Discov.* **7**, 462–477 (2017).
26. Verissimo, C. S. et al. Targeting mutant RAS in patient-derived colorectal cancer organoids by combinatorial drug screening. *eLife* **5**, e18489 (2016).
27. Regot, S., Hughey, J. J., Bajar, B. T., Carrasco, S. & Covert, M. W. High-sensitivity measurements of multiple kinase activities in live single cells. *Cell* **157**, 1724–1734 (2014).
28. Komatsu, N. et al. Development of an optimized backbone of FRET biosensors for kinases and GTPases. *Mol. Biol. Cell* **22**, 4647–4656 (2011).
29. Kamioka, Y. et al. Live imaging of protein kinase activities in transgenic mice expressing FRET biosensors. *Cell Struct. Funct.* **37**, 65–73 (2012).
30. Goedhart, J. et al. Structure-guided evolution of cyan fluorescent proteins towards a quantum yield of 93%. *Nat. Commun.* **3**, 751 (2012).
31. Komatsubara, A. T., Matsuda, M. & Aoki, K. Quantitative analysis of recombination between YFP and CFP genes of FRET biosensors introduced by lentiviral or retroviral gene transfer. *Sci. Rep.* **5**, 13283 (2015).
32. Vinkenborg, J. L., Evers, T. H., Reulen, S. W., Meijer, E. W. & Merkx, M. Enhanced sensitivity of FRET-based protease sensors by redesign of the GFP dimerization interface. *ChemBioChem* **8**, 1119–1121 (2007).
33. Cost, H., Barreau, P., Basset, M., Le Peuch, C. & Geny, B. Phorbol myristate acetate inhibits phosphoinositol lipid-specific phospholipase C activity via protein kinase C activation in conditions inducing differentiation in HL-60 cells. *Cell Biochem. Funct.* **9**, 263–273 (1991).
34. Bonnet, J., Mayonove, P. & Morris, M. C. Differential phosphorylation of Cdc25C phosphatase in mitosis. *Biochem. Biophys. Res. Commun.* **370**, 483–488 (2008).
35. Franckhauser, C., Mamaeva, D., Heron-Milhavet, L., Fernandez, A. & Lamb, N. J. Distinct pools of cdc25C are phosphorylated on specific TP sites and differentially localized in human mitotic cells. *PLoS ONE* **5**, e11798 (2010).
36. Bao, Z. Q., Jacobsen, D. M. & Young, M. A. Briefly bound to activate: transient binding of a second catalytic magnesium activates the structure and dynamics of CDK2 kinase for catalysis. *Structure* **19**, 675–690 (2011).
37. Holt, L. J. et al. Global analysis of Cdk1 substrate phosphorylation sites provides insights into evolution. *Science* **325**, 1682–1686 (2009).
38. King, C., Sarabipour, S., Byrne, P., Leahy, D. J. & Hristova, K. The FRET signatures of noninteracting proteins in membranes: simulations and experiments. *Biophys. J.* **106**, 1309–1317 (2014).
39. Sparta, B. et al. Receptor level mechanisms are required for epidermal growth factor (EGF)-stimulated extracellular signal-regulated kinase (ERK) activity pulses. *J. Biol. Chem.* **290**, 24784–24792 (2015).
40. Gillies, T. E., Pargett, M., Minguet, M., Davies, A. E. & Albeck, J. G. Linear integration of ERK activity predominates over persistence detection in Fra-1 regulation. *Cell Syst.* **5**, 549–563 (2017).
41. Aoki, K. et al. Propagating wave of ERK activation orients collective cell migration. *Dev. Cell* **43**, 305–317 (2017).
42. Harvey, C. D. et al. A genetically encoded fluorescent sensor of ERK activity. *Proc. Natl Acad. Sci. USA* **105**, 19264–19269 (2008).
43. Dymond, A. W. et al. Metabolism, excretion and pharmacokinetics of selumetinib, an MEK1/2 inhibitor, in healthy adult male subjects. *Clin. Ther.* **38**, 2447–2458 (2016).
44. Gerosa, L. et al. Receptor-driven ERK pulses reconfigure MAPK signaling and enable persistence of drug-adapted BRAF-mutant melanoma cells. *Cell Syst.* **11**, 478–494.e9 (2020).
45. Meerbrey, K. L. et al. The pINDUCER lentiviral toolkit for inducible RNA interference in vitro and in vivo. *Proc. Natl Acad. Sci. USA* **108**, 3665–3670 (2011).
46. de Vries-Smits, A. M., Burgering, B. M., Leevers, S. J., Marshall, C. J. & Bos, J. L. Involvement of p21ras in activation of extracellular signal-regulated kinase 2. *Nature* **357**, 602–604 (1992).
47. Canon, J. et al. The clinical KRAS(G12C) inhibitor AMG 510 drives anti-tumour immunity. *Nature* **575**, 217–223 (2019).
48. Waters, A. M. et al. Evaluation of the selectivity and sensitivity of isoform- and mutation-specific RAS antibodies. *Sci. Signal.* **10**, eaao3332 (2017).
49. Matano, M. et al. Modeling colorectal cancer using CRISPR-Cas9-mediated engineering of human intestinal organoids. *Nat. Med.* **21**, 256–262 (2015).
50. Bertotti, A. et al. A molecularly annotated platform of patient-derived xenografts ('xenopatients') identifies HER2 as an effective therapeutic target in cetuximab-resistant colorectal cancer. *Cancer Discov.* **1**, 508–523 (2011).
51. Hiratsuka, T. et al. Intercellular propagation of extracellular signal-regulated kinase activation revealed by in vivo imaging of mouse skin. *eLife* **4**, e05178 (2015).
52. Lavoie, H. & Therrien, M. Regulation of RAF protein kinases in ERK signalling. *Nat. Rev. Mol. Cell Biol.* **16**, 281–298 (2015).
53. Ambrogio, C. et al. KRAS dimerization impacts MEK inhibitor sensitivity and oncogenic activity of mutant KRAS. *Cell* **172**, 857–868 (2018).
54. Hunter, J. C. et al. Biochemical and structural analysis of common cancer-associated KRAS mutations. *Mol. Cancer Res.* **13**, 1325–1335 (2015).
55. Sheffels, E., Sealover, N. E., Theard, P. L. & Kortum, R. L. Anchorage-independent growth conditions reveal a differential SOS2 dependence for transformation and survival in RAS-mutant cancer cells. *Small GTPases* **12**, 67–78 (2019).
56. Nichols, R. J. et al. RAS nucleotide cycling underlies the SHP2 phosphatase dependence of mutant BRAF-, NF1- and RAS-driven cancers. *Nat. Cell Biol.* **20**, 1064–1073 (2018).
57. Mainardi, S. et al. SHP2 is required for growth of KRAS-mutant non-small-cell lung cancer in vivo. *Nat. Med.* **24**, 961–967 (2018).
58. Durrant, D. E. & Morrison, D. K. Targeting the Raf kinases in human cancer: the Raf dimer dilemma. *Br. J. Cancer* **118**, 3–8 (2018).
59. Blasco, R. B. et al. c-Raf, but not B-Raf, is essential for development of *K-Ras* oncogene-driven non-small cell lung carcinoma. *Cancer Cell* **19**, 652–663 (2011).
60. Uhlitz, F. et al. A census of cell types and paracrine interactions in colorectal cancer. Preprint at *bioRxiv* https://doi.org/10.1101/2020.01.10.901579 (2020).
61. Lupo, B. et al. Colorectal cancer residual disease at maximal response to EGFR blockade displays a druggable Paneth cell-like phenotype. *Sci. Transl. Med.* **12**, eaax8313 (2020).
62. Zanella, E. R. et al. IGF2 is an actionable target that identifies a distinct subpopulation of colorectal cancer patients with marginal response to anti-EGFR therapies. *Sci. Transl. Med.* **7**, 272ra212 (2015).
63. Khambata-Ford, S. et al. Expression of epiregulin and amphiregulin and K-ras mutation status predict disease control in metastatic colorectal cancer patients treated with cetuximab. *J. Clin. Oncol.* **25**, 3230–3237 (2007).

Methods

Reagents. The EGF was sourced from Invitrogen, selumetinib, afatinib, lapatinib, lapatinib, gefitinib, erlotinib, SHP099 and LY3009120 from SelleckChem, SCH772984 from MedChemExpress, PMA, nocodazol and CP-724714 from Sigma-Aldrich, RO-3306 from Tocris Bioscience and AMG-510 from MedChemExpress.

Plasmids and cell line construction. Cloning was performed using an In-Fusion HD cloning kit (Clontech Laboratories). The EKAREV biosensor[28] was provided by the Matsuda laboratory and subsequently transferred to miniTol2 vector, including an EF1a promoter and PGK-puromycin-resistance cassette. To substitute eCFP, we inserted gBlock (IDTDNA) encoding Turquoise2 cDNA including dimerization-prone residues and 169 silent mutations (detailed in Extended Data Fig. 4a). For point mutagenesis, including ERK-insensitive control variant T48A, we performed whole-vector PCR starting with mutation-bearing primers. Linker length variants emerged from low-frequency errors in PCR reactions on repetitive repeats in the Eevee-linker of EKAREV.

EKAREV-GW4.0 was developed starting from EKAREV using a four-fragment Multisite Gateway Pro Plus system (Life Technologies). This system allows four separate 'bricks' of the FRET biosensor to be simultaneously transferred to a Destination vector using the Gateway BP and LR recombination reaction. The extended method is described in Sipieter et al. (manuscript in preparation). Alternative ERK1/2 substrates (Alt_ERK_Sub; Extended Data Fig. 4a) were extracted from the literature using the Kinexus website (www.phosphonet.ca/default.aspx) and www.kinasenet.ca. Alternative substrates were further optimized for WW-domain recognition as previously described[64].

To prepare for organoid transgenesis, EKAREV or EKAREN variants were inserted into lentiviral vector containing either ires-Puro or ires-Blast resistance cassette.

ERK-KTR, originally from ref. [27], was first transferred to miniTol2 vector, including an EF1a promoter and blasticidin resistance cassette. Thereafter, its fluorophore was substituted with mCherry through In-Fusion cloning.

For doxycycline-inducible expression of dominant-negative HRas(N17), pInducer20[45] was adapted by insertion (In-Fusion cloning) of HRas(N17), replacing attR1-ORF-attR2 (PCR primers: FW-AgcctactagtccagACGCGTCTCGAGGTCGACaGCTAGCATGgaggagccgcagtc, REV-tcgagcggccgccacGGTAcccgggTCAgtctgagtcaggccC) and subsequent insertion (2-PCR-In-Fusion cloning) of mKate2-NLS (mKate2-FW-cctactagtccagACGCGTTTCcaccATGGTGAGCG, mKate2-REV-gtacagctcAGCGCTAACTTTTCGCT, NLS-FW-GTTAGCGCTCCAAAaAAGAAaaggAA AGTcAGCatGTTAACggagctgtacaaggctagagatat, NLS-REV-gcggctcctccaTGCTAGCAGGTCCAGGGTTCTCTTCAAC).

EKAREN4 and EKAREN5 in miniTol2 and lentiviral plasmids, as well as the inducible pInducer20-mKate2-NLS-P2A-HRas(N17) were deposited at Addgene.

Cloning primers. PCR primers for In-Fusion cloning were as follows:

EKAREV to miniTol2 empty vector:
FW-TCTAGCTAGAGGATCCGCCACCATGGTGAGCAAGGGCGAG and
REV-TCACTATAGTTCTAGaccgtcgacTTACACCTTACGC.

mCherry into ERK-KTR:
FW-ATTCCCATCCaccggtGTGAGCAAGGGCGAGGAG and
REV-ATGGCACTAGGCTAGcTCTAGACTTACTTGTACAGCTCGTCCATGC.

Mutagenesis forward primers (used with reverse complementary counterparts) were as follows:

K424P (on EKAREV):
GATGTCCCTAGAACTCCAGTGGATCCAgcaaagctgtcaTTCCAATTTCC.

K426W (on EKAREV): GATGTCCCTAGAACTCCAGTGGATAAAgcaTGG-ctgtcaTTCCAATTTCCGggcg.

K424P + K426W (on EKAREV): GATGTCCCTAGAACTCCAGTGGATCCAg caTGGctgtcaTTCCAATTTCCGggcg.

PWE (on PW):
ACTCACCATgcggccgccCGGAAATTGGAAtgactcCCAtgctggATCCACTGGAG.

PWW (on PW):
ACTCACCATgcggccgccCGGAAATTGGAAtgaccaCCAtgctggATCCACTGGAG.

PWT (on PW): ACTCACCATgcggccgccCGGAAATTGGAAtgacag CCAtgctggATCggtTGGAGTTCTAGGGACATCTGGtcc.

TA (on EKAREV): ccggaCCAGATGTCCCTAGAgCTCCAGTGGATAAAgcaa.

TA (on PW): ccggaCCAGATGTCCCTAGAgCTCCAGTGGATccagcaTG.

All constructs were sequenced before use.

Cell culture and transfection. RASless MEFs[48] were provided by the Voest laboratory, NKI, Amsterdam. Cells were cultured in Dulbecco's modified Eagle's medium (DMEM), supplemented with 10% fetal calf serum and penicillin/streptomycin (P/S, Lonza). To generate stable lines, RASless MEFs, HEK293 or HeLa cells were co-transfected (using XtremeGENE transfection reagent, Merck) with miniTol vectors encoding FRET sensor variants, together with a vector encoding transposase. Cells were selected using puromycin (0.5 μg ml^{-1}) or blasticidin (10 μg ml^{-1}). Monoclonal lines were generated by picking islands from 10-cm dishes, ~2 weeks after seeding at ultra-low density. For microscopy experiments, cells, either transiently transfected with or stably expressing biosensor variants, were seeded in glass-bottomed dishes (Willco Wells) or 4×-segmented glass-bottomed dishes (Greiner Bio-One).

Patient-derived organoid culture, mutagenesis and maintenance. The collection of colorectal tissue for the generation of CRC organoids was performed according to the guidelines of the European Network of Research Ethics Committees (EUREC) following European, national and local law. In all cases, patients signed informed consent after ethical committees approved the study protocols. Organoids identified by HUB codes *HUB-02-B2-040* (*BRAF^{V600E}*(*#3*)), *HUB-02-B2-096* (*BRAF^{V600E}* (*#4*)), *HUB-02-B2-113* (*KRas^{G12D}*) and *HUB-02-B2-074* (*WT*(*#2*)) are catalogued at https://huborganoids.nl/ and can be requested at info@huborganoids.nl. Distribution to third (academic or commercial) parties will have to be authorized by the Biobank Research Ethics Committee of the University Medical Center Utrecht (TCBio) at request of Hubrecht Organoid Technology (HUB).

CRC PDOs with identifiers p6T (KRas^{G12C}), p9T (KRas^{G12V}), p25T (NRas^{Q61H}), p19bT (BRaf^{V600E}(#2)) and p18T (WT #1) were obtained from a previous study[23]. p1T4 (BRaf^{V600E}(#1)) was obtained from a previous study[65]. These PDOs are not catalogued in the HUB Biobank. See Supplementary Table 1 for an extensive description of organoid lines nomenclature, catalogue numbers and recurrent cancer mutations.

Human CRC organoids were cultured as previously described[23]. In short, organoids were cultured in drops of Matrigel (Corning), and the medium was refreshed every two days. CRC culture medium contained advanced DMEM/F12 (Invitrogen) with 1% P/S (Lonza), 1% HEPES buffer (Invitrogen) and 1% Glutamax (Invitrogen), 10% R-spondin conditioned medium, 10% Noggin conditioned medium, B27 (Invitrogen), 1.25 mM *n*-acetyl cysteine (Sigma-Aldrich), 10 μM nicotinamide (Sigma-Aldrich), 500 nM A83-01 (Tocris), 10 μM SB202190 (ApexBio) and medium was supplemented with 50 ng ml^{-1} EGF (Invitrogen) unless indicated otherwise. Organoids were split via shear stress (pipetting) and/or trypsin-EDTA (Sigma-Aldrich) treatment. Directly after trypsinization, culture medium was supplemented with 10 μM Y-27632-dihydrochloride to prevent anoikis. Organoids were infected with lentivirus encoding EKAREN variants linked to puromycin or blasticidin resistance (for example, pLV-EKAREN5-ires-Puro). Infected organoids were selected using 2 μg ml^{-1} puromycin or 30 μg ml^{-1} blasticidin and grown out as polyclonal populations.

Cell line and PDO line identification. Identities of Rasless MEFs were verified through PCR amplification of cDNA followed by Sanger sequencing. KRAS variants: FW-GACTGAATATAAACTTGTGGTAGTTGGAGCT, REV-TGTTTTCGAATTTCTCGAACTAATGTATAGAAGGC; nested-SEQ-TGCTGATGTTTCAATAAAAGGAATTCCATAACTTCTTG. NRAS: FW-GAGTACAAACTGGTGGTGGTTGGAG, REV-CATCACCACACATGG CAATCCC; nested-SEQ-CCCTGTCTGGTCTTGGCTG.

Identity PDOs were Sanger sequence-verified per point mutations in either TP53 (amplicon1: ACAACCAGGAGCCATTGTCTT and CCTCCCCTGCTT GCCAC; amplicon 2: CTGTGCAATAGTTAAACCCATTT and CAGCAGCTCC TACACCG), KRAS (amplicon: CCGCAGAACAGCAGTCTG and TGATGTCA CAATACCAAG; sequence primer CACCGATACACGTCTGCAGTCAAC), NRAS (amplicon: GCAATTTGAGGGACAAACC and CCTCTCTGAAATTCCTTCG; sequence primer GTCATTCCCAGTAGCAAG) and BRAF (amplicon: CTTCA TAATGCTTGCTCTG and GCCTCAATTCTTACCATC; sequence primer CCTGCCTTAAATTGCATAC).

Western blot assay. Before cell lysis, organoids were incubated with 1 mg ml^{-1} dispase II (Invitrogen) for 10 min at 37 °C to digest Matrigel. Western blot samples for phosphorylated ERK and MEK were lysed using RIPA buffer (50 mM Tris-HCl pH 8.0, 150 mM NaCl, 0.1% SDS, 0.5% Na-deoxycholate, 1% NP-40) containing complete protease inhibitors (Roche). Protein content was quantified using a BCA protein assay kit (Pierce) and analysed by western blot analysis. Membranes were blocked and probed with 1:1,000 diluted antibodies directed against pEGFR(Y1068) (Cell Signaling, cat. no. 2234), EGFR (Cell Signaling, cat. no. 4267), Ras (BD Biosciences, RRID:AB_397425), pMEK1/2 (Ser217/221) (Cell Signaling, cat. no. 9121, RRID:AB_331648), MEK1/2 (Cell Signaling, cat. no. 9122, RRID:AB_823567), ERK1/2 (Cell Signaling, cat. no. 4695, RRID:AB_390779), pERK1/2(Thr202/Tyr204) (Cell Signaling, cat. no. 4370, RRID:AB_2315112) and vinculin (Sigma-Aldrich, cat. no. V9131, RRID:AB_477629).

3D crystallographic analysis. Figure 1c was generated based on PDB entry 3QHW using the programs Molscript[66] and Raster3D[67].

2D (FRET) microscopy on cell lines. For 2D microscopy experiments, cells were seeded on 35-m- diameter glass-bottomed wells and placed on a Leica SP8X inverted laser scanning confocal microscope, equipped with a ×63 oil immersion objective (numerical aperture (NA) of 1.4) or ×40 water immersion objective (NA 1.10) and HyD avalanche detectors. The microscope was continuously held at 37 °C and the sample was supplied with humidified air containing 6% CO_2.

To perform FRET time-lapse imaging, cells were excited with a 458-nm argon laser line and donor and acceptor emissions were detected at 462–505 nm and 508–550 nm, respectively. ERK-KTR-mCherry was excited by the tunable white light laser (WLL), tuned at 585 nm, with detection at 592–700 nm. Leica automated focus control was applied to ensure that cells were cross-sectioned at constant height, also during drug administration through pipetting. For direct comparison of different cell lines under identical experimental conditions, cells were seeded in separate compartments of (4×) segmented glass-bottomed wells (Greiner Bio-one).

In the search for alternative ERK1/2 substrates (Extended Data Fig. 2a,b), cells were positioned on the microscope 30 min before experimentation. The first 10 min of imaging provided basal activity levels. Upon pathway activation, images were acquired for 20 min plus 40 min if inhibitors were subsequently added. Images were acquired at 2-min intervals for characterization of biosensor performance and each 4 min to monitor biosensor behaviour during mitosis. For FRET ratiometric measurements of the EKAR-GW4.0 biosensor and its derivatives, widefield images were captured with a Nikon TiE inverted microscope with a ×20 objective (NA 0.5), a DS-Qi2 CMOS camera and NIS-Elements acquisition software using the JOBS module (Nikon). Ratio imaging used a 440/30-nm excitation filter, a t440/510/575rpc multi-band dichroic mirror and two emission filters (ET480/40 M (CFP) and AT545/30 M (YFP)). Lumencor provided excitation filters and all dichroic mirrors and emission filters were from Chroma Technology. An automated emission filter wheel Lambda 10-B Smart Shutter was sourced from Sutter Instrument. The YFP/CFP ratio was calculated per pixel on background-subtracted images, using custom routines (MatLab or NIS Element)

Correlated FRET acquisition and immunofluorescence staining. To 'benchmark' the detection range of EKAREN5 to conventional ppERK staining, HeLa cells stably expressing EKAREN5 were seeded on cover slips with a 500-µm grid (Ibidi) two days before and serum-starved one day before the experiment. Cells were FRET time-lapsed as described above (1 frame per minute). Fixation (paraformaldehyde, 4%, 20 min at room temperature) was performed instantly after acquisition. After permeabilization and immunostaining using primary antibody against ppERK1/2 (Thr202/Tyr204; Cell Signaling Technology, 4370S (RRID:AB_2315112); overnight, 1:250 at room temperature; blocking solution 2% bovine serum albumin, 10% normal goat serum and 50 mM ammonium chloride in PBS) and secondary anti-rabbit antibody, conjugated to AlexaFluor568. Grid coordinates were used to (retro)-identify cells and image them using the Leica SP8 CLSM. Segmentation of nuclei was performed based on sensor (YPet) fluorescence. The signal (FRET and IF) was quantified from individual cells unless discarded (if unhealthy, multi-nucleated, mitotic, suboptimally trans-sectioned).

3D FRET microscopy in patient-derived organoids. PDOs were trypsinized and deposited in 15-µl drops of Matrigel on glass-bottomed dishes (Willco Wells). Seven days later, these were placed on the aforementioned Leica SP8X microscope (×40 water, NA 1.1, 37 °C, 6% CO_2) using resonant scanning (8,000 Hz), thereby drastically reducing the phototoxic burden on the sample[68]. Short dwell times were compensated by frame averaging (×50). Excitation/emission settings were as described for 2D FRET imaging. Approximately 10–20 organoids with medium EKAREN5 expression were analysed using the multiple-position mode, *z* stacks of ~8×2-µm steps, and 2- and 4-min time intervals. All in all, overnight PDO imaging was performed without signs of photobleaching.

To analyse drug responses, PDOs were seeded in 4×-segmented glass-bottomed dishes. Alternatively, to compare drug responses between different PDO lines, each was deposited in clearly separated drops of Matrigel on a glass-bottomed dish, to ensure identical treatment conditions.

For calibration, full pathway inhibition was enforced by selumetinib (5 µM) and SCH772984 (5 µM). After multiple washing steps, full pathway activation was enforced by PMA (150 nM) and, subsequently, phosphatase inhibitor OA (1 µM). Single-cell max-FRET ratios (at saturation/plateau) could consistently be derived before cell death. Before the administration of PMA and OA, inhibitors were washed out manually using two simple syringes and tubing (BioRad), one to remove inhibitor and the other to replenish, thereby reducing inhibitor concentrations to negligible amounts within 1 min. Leica's 'Best Focus' function based on glass reflection was employed to correct movements in the *z* direction. Double normalization of the final FRET traces was performed only if super-activation induced a plateau level reflecting sensor saturation.

FRET ratios are designated 'YFP/CFP' on the *y* axes, referring to the classical fluorophore couple (rather than YPet/Turquoise2).

Multimodal FRET analysis macro. A custom-made FRET analysis macro was generated in ImageJ/Fiji. The basic architecture requires loading of imaging data, background subtraction, optional cropping (in *XY* and/or time), optional de-jittering, optional pixel shift correction and user-guided thresholding to set background pixels to NaN. Next, scripted loops enable multiple analyses from these pre-processed channels ad infinitum, for example for consecutive analysis of single cells. Analyses are defined by regions of interest (ROIs), manually generated by either automated cell tracking, manual drawing, intensity-based thresholding or combinations thereof. Automated cell tracking includes watershedding for particle separation. Manual drawing includes ImageJ's 'ROI interpolation' function. A minimum of drawn ROIs are 'morphed' to cover all time points. Drawing can be performed loosely, because undesired pixels from neighbouring cells and nuclei can be automatically cleared. Intensity-based thresholding can be performed based on any channel and can be varied over the time course. Finally, defined ROI sets can be 'shrunk' to exclude artefact-prone pixels bordering the nuclei, possibly resulting from out-of-focus emission light.

Output ratio traces are calculated as [ROI-mean-acceptor-fluo]/[ROI-mean-donor-fluo] per time point. By default, the saved outputs are (1) videos (avi-format) combining fluorescence image, FRET image, generated ROIs and traces, thus allowing association of features of the FRET trace to cellular behaviour and/or pharmacological interferences (for example, Supplementary videos), (2) snapshots (same design, jpeg) for efficient archiving and (3) Excel documents, containing all raw readout data, for example, absolute FRET ratios, baseline-normalized and double-normalized ratios. For the latter, the user can indicate time intervals as reference values for normalization, for example intervals representing the fully inhibited ERK pathway and the fully activated ERK pathway.

To ensure optimal cross-sectioning of single cells through time in 3D EKAREN5 PDOs (*XYZT*), we generated the 'plane-picking' tool. In short, by simultaneous visualization of consecutive confocal *z* planes (zoomed around the cell of choice), this allows precise picking of optimal *z* planes over consecutive time intervals. The extraction of 'picked planes' from the *XYZT* dataset yields an *XYT* time-lapse, ready for all the above-mentioned analyses. Cells with substantial movement in *z* (>8 µm) were rare, but were excluded when encountered. Although our ImageJ/Fiji-based script may not compete with professional software packages in terms of automated segmentation, calculation power and speed, in our hands it appeared the safest and best-controlled method to derive single-cell traces, free of artefacts.

Besides single-cell analyses, we also performed 'plane analyses', that is, determination of the overall FRET activity level per organoid. Pooling the signal from all cells in such organoid trans-sections favours high signal to noise, suitable for quantitative determinations.

Recording and analysis of ERK fluctuations in double-sensor HeLa cells (KTR + FRET). Clonal HeLa cell lines were generated with comparable ERK-KTR-mCherry and FRET sensor expression (Extended Data Fig. 2e). Cells were seeded in identical densities on fibronectin-coated 4×-segmented glass-bottomed dishes (Greiner Bio-One) and imaged under serum for 18 h. KTR and FRET signals were simultaneously recorded in three cell lines (KTR + either EKAREV or EKAREN4 or EKAREN5) under identical experimental conditions.

Single-cell FRET-ratio plots were derived as described above. Image analysis was extended to the ERK-KTR-mCherry sensor. Nuclear ROIs, determined by nuclear EKAREV, were used to discriminate nucleus from cytosol. Output ratio values were calculated as [mean-fluo-in-cytosol]/[mean-fluo-in-nucleus] per time point.

Traces were normalized to baseline values and subjected to a sliding averaging procedure in Excel prior to visual inspection. To focus on fluctuations within a defined amplitude range, traces were plotted at invariable scaling, that is, within the raster size of constant units (KTR, units of 0.05; FRET, units of 0.005; Fig. 2e). Traces were scrutinized for KTR deviations of predetermined amplitude and subsequently evaluated to establish whether these ERK fluctuations were mirrored by the FRET signal. The scores represent the percentage of KTR peaks co-recognized by the FRET signal per single-cell recording (recordings containing <3 KTR peaks were excluded).

Various automated analyses were performed to corroborate the visually scored results. Peak numbers were counted using a freely available MatLab script (MathWorks, Signal Processing Toolbox, R2018a) and, for comparability, scores were normalized to the peak numbers counted in ERK-KTR traces (Extended Data Fig. 3e). To compare the upward and downward movements of signal changes, we studied first derivatives of all traces (Excel) and assessed the percentage of time frames wherein both signal changes were positive (Extended Data Fig. 3f) or negative (Extended Data Fig. 3g). Finally, we studied the signal versatility by counting 'inflection' points (Excel), which we defined as frames where the second derivative crosses zero (Extended Data Fig. 3h). All scores were normalized to ERK-KTR traces.

Long-term growth assessment in CRC PDOs. Five-day-old EKAREN5 PDOs were dissociated from Matrigel using dispase, size-filtered (40-µm pore) and replated in glass-bottomed 96-well plates (Ibidi, cat. no. 89646). *XYZ* imaging was carried out at the indicated time points with the SP8X Leica CSLM (×10, dry, NA 0.4), resonant scanning (8,000 Hz) and 514 nm (argon laser) excitation. Each pharmacological condition was repeated in three wells, with four *z*-stack (15×12 µm) acquisitions (positions) per well (thus 12 *z* stacks per condition). Per time point, the same positions were scanned. The organoid number per time point (frequently >100) is indicated in the figures (or legends).

For analysis, 3D stacks were maximum-projected and subjected to heavy Gaussian blurring (ImageJ/Fiji script) before the automated detection and size measurement of individual organoids (Columbus, Perkin-Elmer).

Immunohistochemistry in PDX-derived tumour tissue. Formalin-fixed, paraffin-embedded tumour material from NOD (nonobese diabetic)/SCID (severe combined immunodeficient) mice (in compliance with all relevant ethical

regulations) from a previous study[50] were used and subjected to immunoperoxidase staining with rabbit anti-phospho-ERK (Thr202/Tyr204)(D13.14.4E) (Cell Signaling cat. no. 4370).

After incubation with DakoEnVision+ System- HRP-labelled polymer anti-rabbit secondary antibody (Dako cat. no. K4002), immunoreactivity was revealed by incubation in DAB chromogen (Dako) and sections were counterstained with haematoxylin. Images were captured with the Leica LAS EZ software using a Leica DM LB microscope. Morphometric quantitation was performed with ImageJ software using spectral image segmentation. Software outputs were manually verified by visual inspection of digital images.

Statistics and reproducibility. The results presented are representative of two or three independent experiments, unless otherwise indicated. Student's *t*-tests were carried out using Microsoft Excel to calculate significance. Differences were considered significant at $*P<0.05$, $**P<0.005$ or $***P<0.0005$. Regression coefficients were calculated in Microsoft Excel. Results are expressed as mean ± standard deviation (s.d.) unless indicated otherwise.

In exceptional cases, biological replicate experiments yielded results of subtle variation, without affecting the general interpretation of the aimed research question. First, the dampening effect of selumetinib on autonomous ERK activity oscillations (Fig. 3b) was consistently observed, but formally the individual experiments were intentionally performed at variable selumetinib concentrations (Extended Data Fig. 6), resulting in alternative frequencies of ERK reactivation. Second, comparison of EKAREN4 with EKAREN5 (Extended Data Fig. 3a) consistently showed a subtle decrease in FRET span ($n=2$), while the regression coefficients describing the effects of expression level were not exact copies.

Reporting Summary. Further information on research design is available in the Nature Research Reporting Summary linked to this Article.

Data availability

Source data are provided with this paper. All other data supporting the findings of this study are available from the corresponding author on reasonable request.

Code availability

Custom-written ImageJ/Fiji-scripts that were used to analyse 2D and 3D FRET data are available from the corresponding author upon request.

References

64. Huang, Y. M. & Chang, C. E. Mechanism of phosphothreonine/serine recognition and specificity for modular domains from all-atom molecular dynamics. *BMC Biophys.* **4**, 12 (2011).
65. Roerink, S. F. et al. Intra-tumour diversification in colorectal cancer at the single-cell level. *Nature* **556**, 457–462 (2018).
66. Kraulis, P. J. Similarity of protein G and ubiquitin. *Science* **254**, 581–582 (1991).
67. Merritt, E. A. & Murphy, M. E. Raster3D Version 2.0. A program for photorealistic molecular graphics. *Acta Crystallogr. D Biol. Crystallogr.* **50**, 869–873 (1994).
68. Borlinghaus, R. T. MRT letter: high speed scanning has the potential to increase fluorescence yield and to reduce photobleaching. *Microsc. Res. Tech.* **69**, 689–692 (2006).

Acknowledgements

We thank members of the Snippert, Riquet and Trusolino laboratories for reagents, suggestions and discussions. We thank M. Gloerich for careful reading of the manuscript. This work is part of the Oncode Institute, which is partly financed by the Dutch Cancer Society and was funded by the Gravitation Program CancerGenomics.nl from the Netherlands Organisation for Scientific Research (NWO), by a grant from the Dutch Cancer Society (KWF/UU2013-6070, H.J.G.S.), ERC starting grant (IntratumoralNiche, H.J.G.S.) and a 'Sta op tegen Kanker' International Translational Cancer Research grant (J.L.B.). Stand Up to Cancer is a programme administered by the AACR. Research was further supported by EOS MODEL-IDI (FWO grant no. 30826052), iBOF ATLANTIS (BOF20/IBF/039), FWO research grants (G.0E04.16N, G.0C76.18N, G.0B71.18N and G.0B96.20N), Methusalem (BOF16/MET_V/007), Foundation against Cancer (F/2016/865 and F/2020/1505), CRIG and GIGG consortia, and VIB (to P.V.). This research was supported by the Agence Nationale pour la Recherche (ANR) via the G2Progress programme (ANR-13- BSV2-0016-02, F.B.R.). F.B.R. acknowledges the Nikon BELUX partnership and funding from Oseo–Ministère de l'enseignement supérieur et de la recherche via the national contest 2013 d'aide à la création d'entreprise de technologies innovantes catégorie émergence in the context of the KiBioS spin-off project. This collaborative work was encouraged by the CNRS Groupement de recherche (GDR) 2588 'Microscopie et Imagerie du Vivant' scientific community via the biosensor workgroup initiative and especially during IMOB2018. Additional funding was provided by AIRC (Associazione Italiana per la Ricerca sul Cancro) Investigator grants 20697 (A.B.) and 22802 (L.T.), AIRC 5x1000 grant no. 21091 (A.B. and L.T.), AIRC/CRUK/FC AECC Accelerator Award 22795 (L.T.), European Research Council Consolidator Grant 724748—BEAT (A.B.), H2020 grant no. 754923 COLOSSUS (L.T.), H2020 INFRAIA grant no. 731105 EDIReX (A.B.) and Fondazione Piemontese per la Ricerca sul Cancro-ONLUS, 5x1000 Ministero della Salute 2014, 2015 and 2016 (L.T.). A.B. and L.T. are members of the EurOPDX Consortium.

Author contributions

B.P. and H.J.G.S. conceived and oversaw the project. B.P., J.R.B.d.A., H.R., F.B.R., J.L.B. and H.J.G.S. wrote the manuscript. F.B.R. and P.V. provided grant support and oversaw experiments. B.P., J.B.P., J.L.B., L.T., F.B.R. and H.J.G.S. designed experiments. B.P., R.L.v.I., S.K., J.R.B.d.A., D.L., F. Sipieter and B.C. performed FRET microscopy. J.B.P. and S.M. performed western blots. H.R. analysed crystallography data. A.B. and F. Sassi performed and analysed in vivo experiments. I.V.-K. assisted with organoid culture. R.G.J.V. and S.F.B. provided PDO material.

Competing interests

The authors declare no competing interests.

Additional information

Extended data is available for this paper at https://doi.org/10.1038/s41556-021-00654-5.

Supplementary information The online version contains supplementary material available at https://doi.org/10.1038/s41556-021-00654-5.

Correspondence and requests for materials should be addressed to H.J.G.S.

Peer review information *Nature Cell Biology* thanks the anonymous reviewers for their contribution to the peer review of this work. Peer reviewer reports are available.

Reprints and permissions information is available at www.nature.com/reprints.

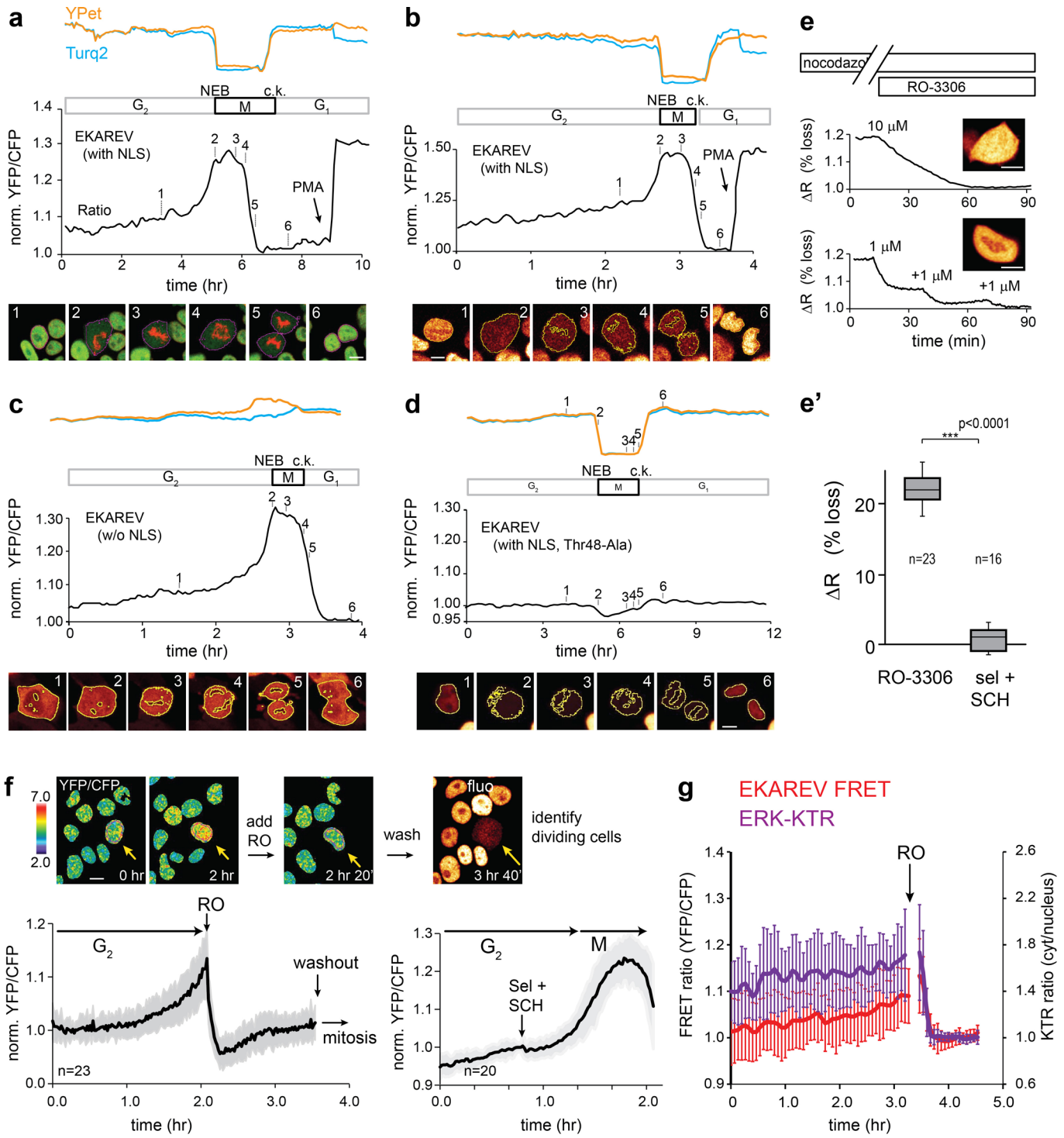

Extended Data Fig. 1 | See next page for caption.

Extended Data Fig. 1 | CDK1/cyclinB phosphorylates EKAREV(Tq) during G_2- and M-phase. a, Typical mitotic EKAREV-FRET profile in HEK293 cells, including rising phase, steep increase at nuclear envelope breakdown (NEB) and sharp decline at anaphase (Supplementary Movie 1). Corresponding snapshots of above cells with H2B-mScarlet support cell-cycle phases (20 cells; 1 experiment). 1, G_2; 2, NEB; 3, metaphase; 4, anaphase; 5, cytokinesis (c.k.); 6, G_1. FRET-signal relative to PMA saturation (150nM). Black, FRET-ratio of YPet(yellow)/Turq2(blue) intensities. **b**, As **a**, with cell-cycle stages recognized by EKAREV(Tq) biosensor exclusion from condensed chromosomes; consistently observed (53 cells, 4 experiments). **c**, As **a**, but EKAREV(Tq) biosensor lacking nuclear localization. Observed in 28 cells, 2 experiments. **d**, As **a**, but EKAREV(TA) control biosensor that cannot be phosphorylated. Observed in 5 cells, 1 experiment. **e**, EKAREV(Tq) FRET signal in mitotic arrested HEK293 cells (nocodazol, 0.83μM; 2hrs) is sensitive to CDK1 inhibitor RO-3306. In mitotic cells, recognized by absence of nuclear localization (NEB) of NLS-tagged biosensor (insert images), FRET decreased upon 10μM RO-3306 (9 cells; 2 experiments with similar results), or 3x 1μM (1 cell). **e'**, Loss of normalized FRET signal (ΔR, %) upon RO-3306 (10μM) or MAPK pathway inhibitors (sel+SCH, 5μM each). Box-and-whisker plots: boxes represent quartile 2 and 3, horizontal line represents median, whiskers represent minimum and maximum within 1,5x interquartile range. RO-3306: n=23 cells, sel+SCH n=16 cells. **f**, EKAREV(Tq) FRET signal is sensitive to CDK1-inhibition in G_2-phase. Synchronized cells were imaged before, during and after incubation with RO-3306 (10μM) and retrospectively analyzed if mitotic entry was observed <15 minutes after drug washout (n=23 cells). Right, similar experiment, here inhibiting MEK and ERK (n=20 cells). Graph shows mean±s.d. of baseline-normalized traces. **g**, As **f**, monitoring G_2-phase in HeLa cells (n=19) co-expressing ERK-KTR-mCherry and EKAREV(Tq). ERK-KTR biosensor suffers from same undesired CDK1-sensitivity. ***, two-sided student's T-test, $p<0.0005$. Scale bar, 10μm.

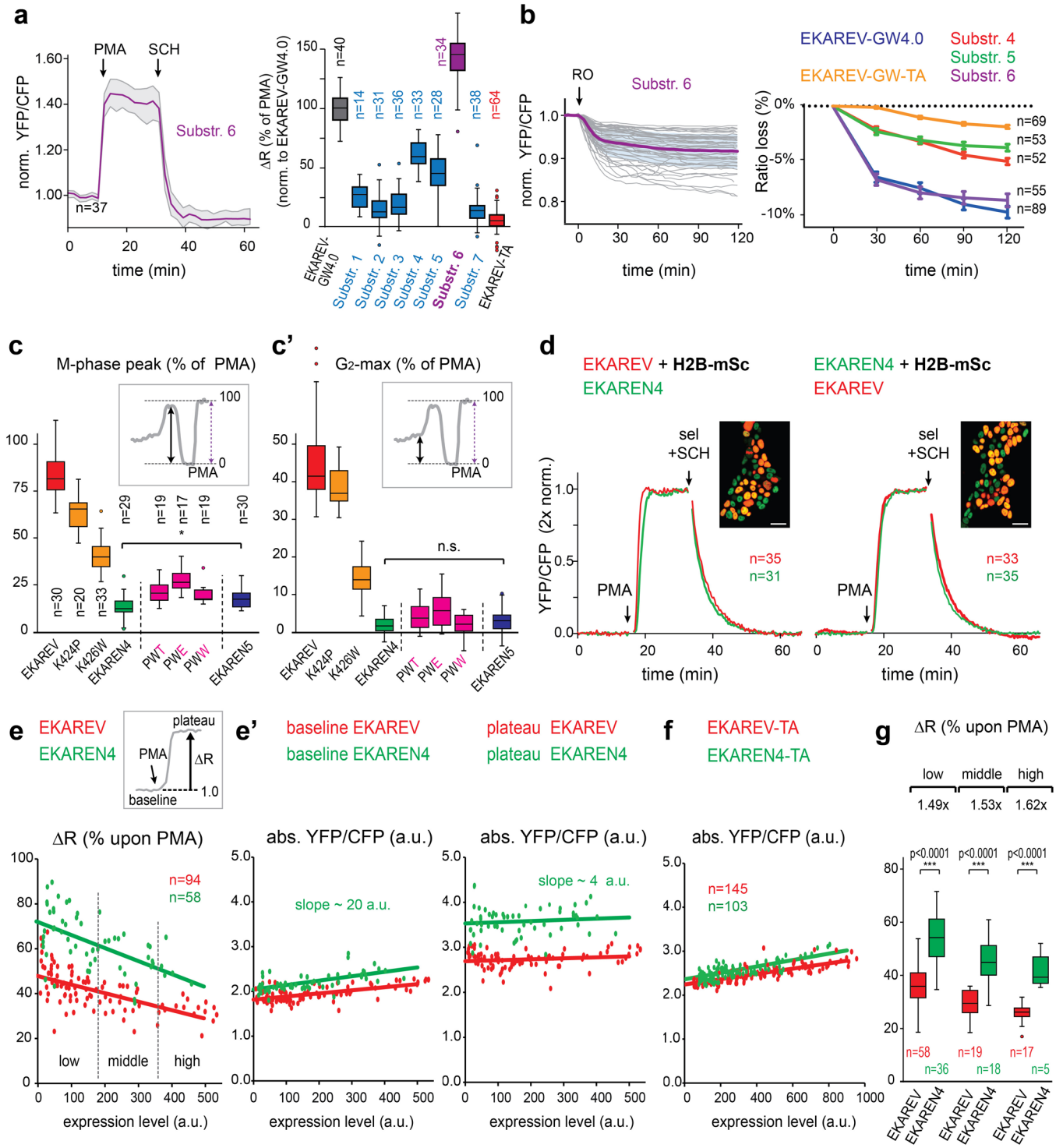

Extended Data Fig. 2 | See next page for caption.

Extended Data Fig. 2 | Improving ERK specificity, generating EKAREN4. a, HeLa cells expressing EKAREV substrate variants Alt_ERK_Substr_1-6 (Extended Data Fig. 4b). PMA, 500nM; SCH, 10μM. Right, responses (mean±s.d.), normalized to EKAREV-GW4.0. **b**, HeLa cells expressing EKAREV-GW variants were arrested in mitosis (Extended Data Fig. 1e) to test CDK1/cyclinB sensitivity (RO-3306). Purple, mean of individual traces. Right, overview for several variants, mean ratio loss ± s.e.m. Best responder EKAREV-GW(Alt_substr._6) is compromised by RO-sensitivity. **c**, Repeat of Fig. 1e, quantifying FRET in G_2- and M-phase HEK293 cells(mean ± s.d), complemented with results from third-residue-substitution variants (purple). No improvements compared to EKAREN4/EKAREN5. **d**, Sensor dephosphorylation kinetics, assessed by instant ERK inactivation (sel+SCH, 5μM) after initial sensor saturation (PMA). For identical experimental conditions, HEK293 stably expressing EKAREV(Tq) or EKAREN4 were mixed. H2B-mScarlet selectively marked EKAREV(Tq) (left) or EKAREN4 cells (right) (insets: scale, 25 μm). Cells analyzed individually and averaged after double normalization (baseline and PMA-plateau). **e**, Maximum FRET range (ΔR(%), approximated through saturation (PMA) in serum-starved HEK293 cells of widely variable expression levels. **e'**, Baseline and plateau ratios corresponding to cells in **e**. Increased FRET range of EKAREN4 likely results from elevated plateau ratios. Expression levels affect FRET range by differentially affecting baseline ratios (see slopes in a.u.). Experiment performed twice. **f**, As **e**, differential effect of expression level on FRET range is similar for ERK-insensitive control sensors EKAREV(TA) and EKAREN4(TA). **g**, Mean (± s.d.) ΔR per expression level category (see **e**). For panels **a-g** the n numbers represent cells and are indicated in the graph for each group. Box-and-whiskers: boxes represent quartile 2 and 3, horizontal line represents median, whiskers represent minimum and maximum within 1,5x interquartile range. Dots are outliers. P values in all relevant panels were calculated using a two-sided student's T-test, * $p<0.05$; ***, $p<0.0005$. n.s., non-significant.

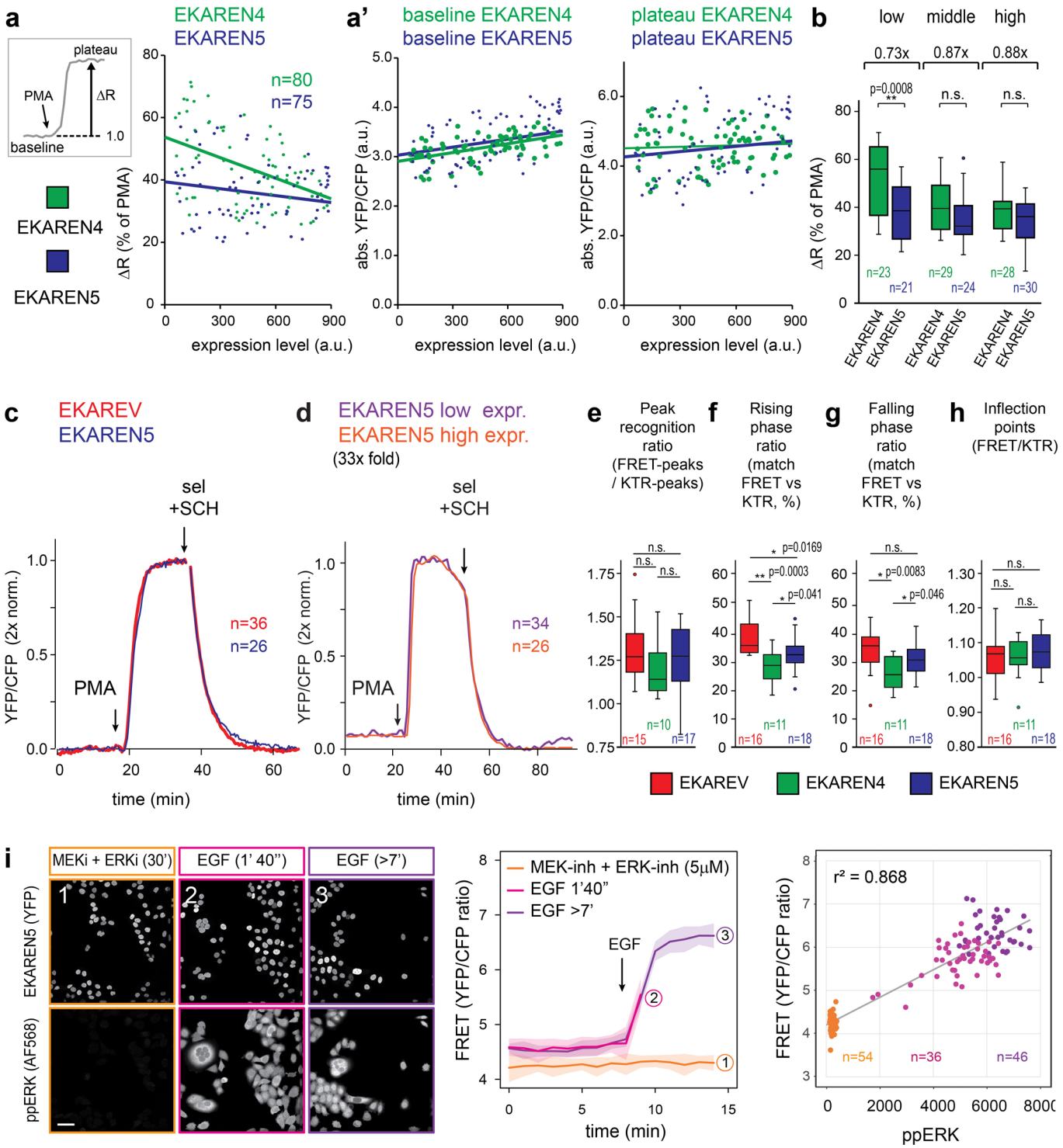

Extended Data Fig. 3 | See next page for caption.

Extended Data Fig. 3 | Multi-dimensional analyses comparing EKAREV, EKAREN4 and EKAREN5. a, FRET-range versus sensor expression level, as in Extended Data Fig. 2e (EKAREN4, n=80 cells; EKAREN5, n=75 cells). **a'**, baseline and plateau ratios corresponding to cells plotted in **a**. **b**, Means (± s.d.) of ΔR from **a**, calculated in three expression level categories (as in Extended Data Fig. 2g). **c**, Dephosphorylation kinetics of EKAREN5 were directly compared with EKAREV(Tq) (as Extended Data Fig. 2d). Retrospective unmixing was based on clustering plateau amplitudes (PMA) (see Fig. 2a). Experiment performed once. **d**, As in **c**, comparing phosphorylation and dephosphorylation kinetics of EKAREN5 with ~33-fold expression level difference. Co-seeded high and low expressors were simultaneously monitored. Experiment performed three times. **e-h**, Various automated analyses on autonomous ERK fluctuations of HeLa cells (dataset of Fig. 2f,g), registered simultaneously by ERK-KTR-mCherry and either of EKAREV/EKAREN FRET sensors. EKAREV, n=15 single-cell traces; EKAREN4, n=10 single-cell traces; EKAREN5, n=17 single-cell traces. **e**, Automated peak counting per individual cell. **f**, Temporal matching of rising phases in KTR versus FRET signals. **g**, Temporal matching of falling phases in KTR versus FRET signals. **h**, Counted 'inflection' points per trace, that is points where ERK changes accelerate or decelerate(see Methods). **i**, Correlation between EKAREN5-FRET and ppERK staining (mean nuclear signal). After various ERK manipulations, HeLa-EKAREN5 cells were FRET-imaged and fixed instantly after acquisition, yielding various ERK activity states between complete inhibition (MEKi+ERKi) and pathway saturation (>7 min EGF). Grey line, regression analysis (y=ax+b). Traces are mean ratios ± s.d. For panels **a-i** the n numbers represent cells and are indicated in the graph for each group. Box-and-whisker plots: boxes represent quartile 2 and 3, horizontal line represents median, whiskers represent minimum and maximum within 1,5x interquartile range. Dots, outliers. Scale bar, 50μm. Two-sided student's T-tests: *, $p<0.05$; **, $p<0.005$; n.s., non-significant.

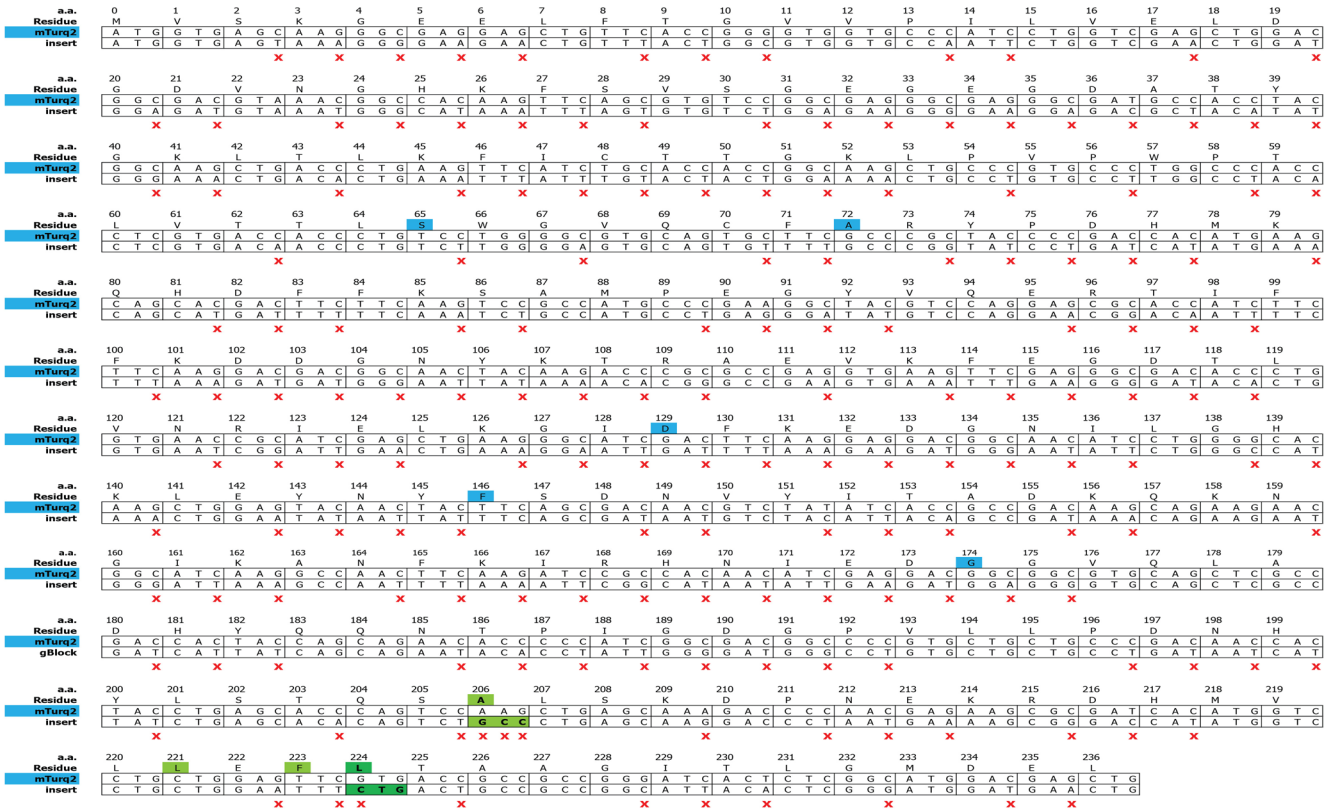

b

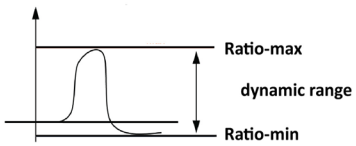

subtle amino acid differences
inactivating mutation
ERK docking site

Code	ERK substrate from…	Amino acid sequence	Mean Difference	Reference
EKAREV-GW 4.0	Cdc25C-T48	PDVPRTPVDKAKLSFQFP	35,82	Harvey et al., PNAS, 2008
Alt_ERK_substrate 1	hRSK1-S363	VTSRAPKDSPGIPPSASFQFP	9,46	Dalby et al., 1998, J Biol Chem
Alt_ERK_substrate 2	hELK1-S383	IHFWSTLSPIAPRAPAKLSFQFP	5,06	Xing J. et al., 1996, Science
Alt_ERK_substrate 3	hELK1-S383/389	SIHFWSTLSPIAPRSPAKLSFQFP	6,74	Klussendorf Thesis, 2011
Alt_ERK_substrate 4	hRSK1-T573	AENGLLMTPCDTANFSFQFP	21,98	
Alt_ERK_substrate 5	hRSK1-T573	AENGLLMTPCYTANFSFQFP	16,43	Dalby et al., 1998, J Biol Chem
Alt_ERK_substrate 6	hRSK1-T359	DTEFTSRTPKDAPGISFQFP	51,13	Dalby et al., 1998, J Biol Chem
Alt_ERK_substrate 7	hELK1-S389	IHFWSTLAPIAPRSPAKLSFQFP	5,06	Gille H. et al., 1995, EMBO
EKAREV TA-mutant	Cdc25C-T48A	PDVPRAPVDKAKLSFQFP	1,79	Komatsu et al., MBoC, 2011

c

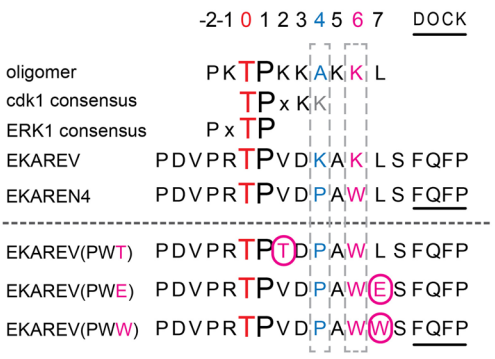

d

EKAREN4-constructs

transposon-based

miniTol2 x EKAREN4-nls	+ PGK x blast/puro
miniTol2 x EKAREN4-nes	+ PGK x blast/puro
miniTol2 x EKAREN4	+ PGK x blast/puro
miniTol2 x EKAREN4-nls(TA)	+ PGK x blast/puro
miniTol2 x EKAREN4(TA)	+ PGK x blast/puro

lentiviral plasmids

pLV x EKAREN4-nls	+ PGK x blast/puro
pLV x EKAREN4-nes	+ PGK x blast/puro
pLV x EKAREN4	+ PGK x blast/puro
pLV x EKAREN4-nls(TA)	+ PGK x blast/puro

EKAREN5-constructs

miniTol2 x EKAREN5-nls	+ ires-blast/puro
miniTol2 x EKAREN5-nes	+ ires-blast/puro
miniTol2 x EKAREN5	+ ires-blast/puro
miniTol2 x EKAREN5-nls(TA)	+ ires-blast/puro
miniTol2 x EKAREN5(TA)	+ ires-blast/puro

pLV x EKAREN5-nls	+ ires-blast/puro
pLV x EKAREN5-nes	+ ires-blast/puro
pLV x EKAREN5	+ ires-blast/puro
pLV x EKAREN5-nls(TA)	+ ires-blast/puro

Inducible d.n.HRas, extended with reporter FP (mKate2-nls)

pInducer20-based lentiviral plasmid

mKate2-P2A-d.n.HRas(N17)	+ ires-puro

Extended Data Fig. 4 | See next page for caption.

Extended Data Fig. 4 | Biosensor sequences. a, Silent mutations introduced into Turquoise2 (insert) to minimize sequence homology with the YPet fluorophore in the same construct. Red 'x' marks silent mutations. Blue, residues discriminating Turquoise2 from parental eCFP (Goedhart et al.[30]). Green, residues rendering Turquoise2 prone to dimerize with YPet, in analogy to EKAREV design (Komatsu et al., 2011[28]). Dark green, the V224L mutation was added to further enhance dimerization and, hence, FRET efficiency in ON-state (Vinkenborg et al., 2007[32]). **b**, Alternative ERK substrate sequences were derived from ERK targets RSK1 (human) and ELK1 (human) using the Kinexus website and compared to parental EKAREV-GW-4.0 (GW = GateWay) with CDC25C substrate sequence. **c**, Overview of generated and tested point mutant variants of EKAREV. Red, central Threonine, target of ERK phosphorylation. Blue, the Lysine at position +4 mimics the general CDK1-consensus site, mutated to Proline (K->P). Purple, the Lysine at position +6 mimics the CDK1-consensus site and mutated to bulky Trp (K->W) to create steric hindrance with cyclinB. Underlined, ERK docking domain FQFP. Purple boxed characters, rational attempts to further eliminate CDK1-sensitivity with third amino acid replacements. V422T was aimed at favoring ERK over CDK1 consensus site; L427W was aimed at further augmenting sterical hinderance of cyclinB interaction; L427E was aimed at impeding cyclinB interaction through electrostatic repulsion. The Asp (D) at position+3 was left unchanged for its reported importance for the Pin1 affinity (Komatsu et al., 2011[28]). **d**, Summary of available EKAREN4 and EKAREN5 plasmid constructs (including variable targeting motifs and Thr-Ala control versions), as well as adapted version of pInducer20 (Meerbrey et al., 2011[45]) to initiate expression of $HRAS^{N17}$ and P2A-coupled reporter fluorophore mKate2-NLS. Constructs were deposited at Addgene.

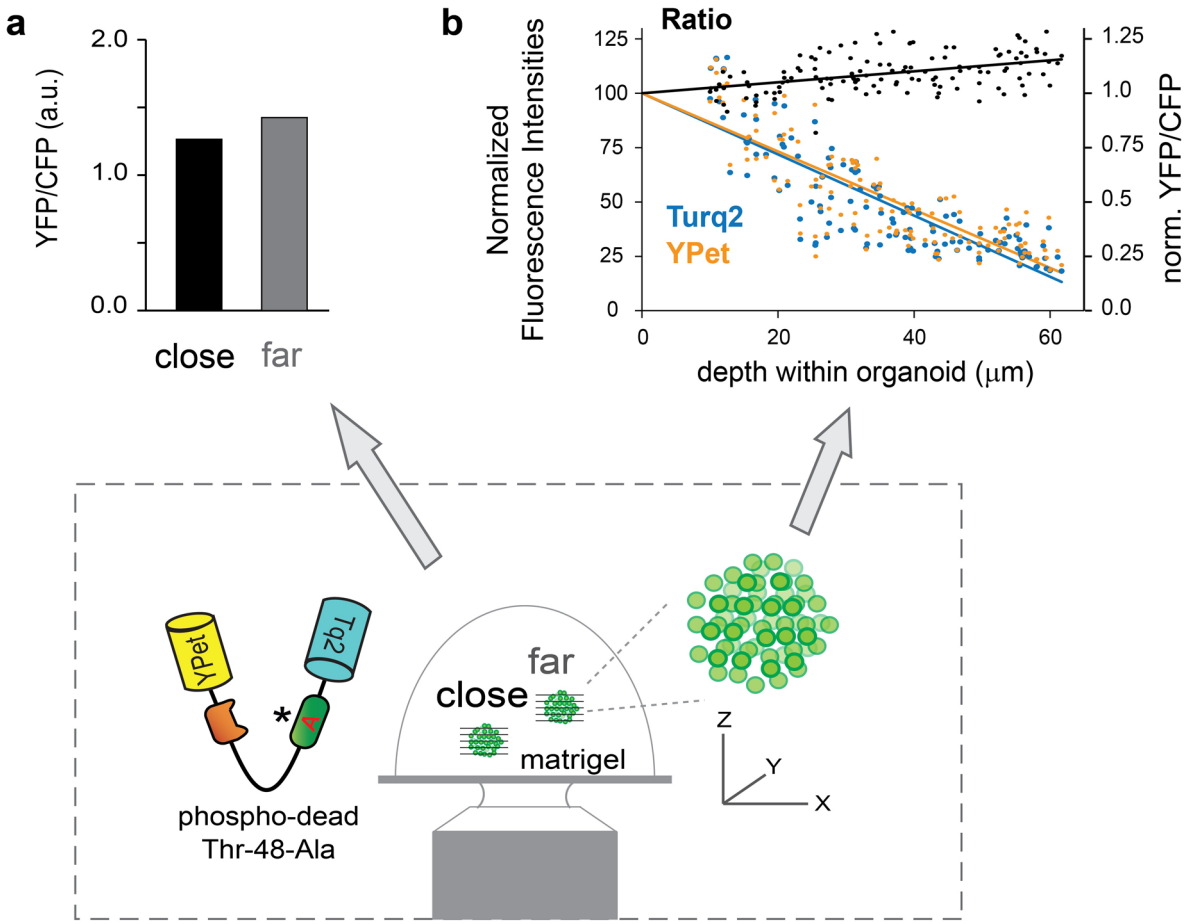

Extended Data Fig. 5 | Geometric effects on raw FRET signals in 3D organoid models. a, PDO model expressing the non-phosphorylatable (hence ERK-insensitive) control sensor EKAREV(TA) was FRET-imaged to assess non-biological geometry effects on raw signals in 3D organoid FRET microscopy. YFP/CFP ratios can differ between organoids situated either far away or close to the objective (distance difference ~150 μm). Experiment performed once, this direct comparison representing general observations. **b**, Performing FRET acquisition, Turq2 and YPet emissions were determined from all cells of a bulky organoid (>200 cells) and plotted against their z-coordinates. YFP/CFP ratios increase subtly with increasing depth within the organoid, likely due to differential scattering-induced loss of fluorescence between the two fluorophores. Experiment performed twice with same outcome.

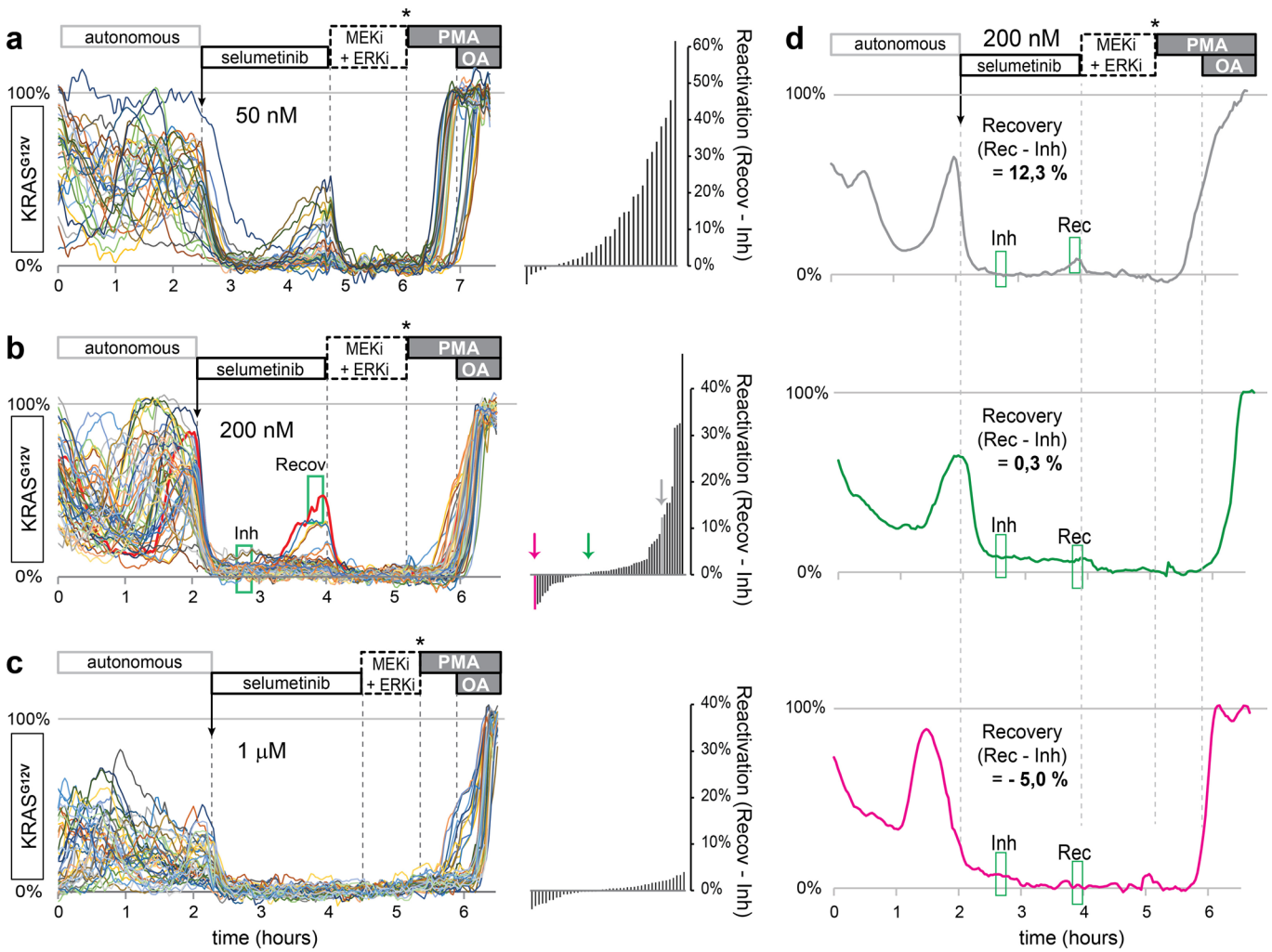

Extended Data Fig. 6 | Single-cell ERK responses in organoids to various doses of selumetinib. a, As in Fig. 3b, here using selumetinib at 50 nM concentration. Shown are 33 single-cell analyses from two p9T organoids. Right, waterfall plot summarizing cellular recovery from ERK inhibition (see also Fig. 3b). **b**, Exact copy of Fig. 3b, using selumetinib at 200 nM concentration. Shown are 59 single-cell analyses from three p9T organoids. Right, waterfall plot summarizing the cellular recovery from ERK inhibition. **c**, As in Fig. 3b, here using selumetinib at 1 µM concentration. Shown are 42 single-cell analyses from three p9T organoids. Right, waterfall plot summarizing the recovery from ERK inhibition. **d**, Three example FRET traces to illustrate the power of time-resolved signal transduction analysis. Trace colours correspond to bars indicated with coloured arrows in waterfall plot of **c**. Top, cell displaying onset of recovery, interrupted by super-inhibition. Middle, selumetinib-induced inhibition is followed by a sustained phase without apparent recovery. Bottom, inhibitory effect is more prolonged, explaining negative outcome for Recovery (= 'Recov' – 'Inh'). Grey, green and purple colours correspond with bars in waterfall plot of Extended Data Fig. 6b.

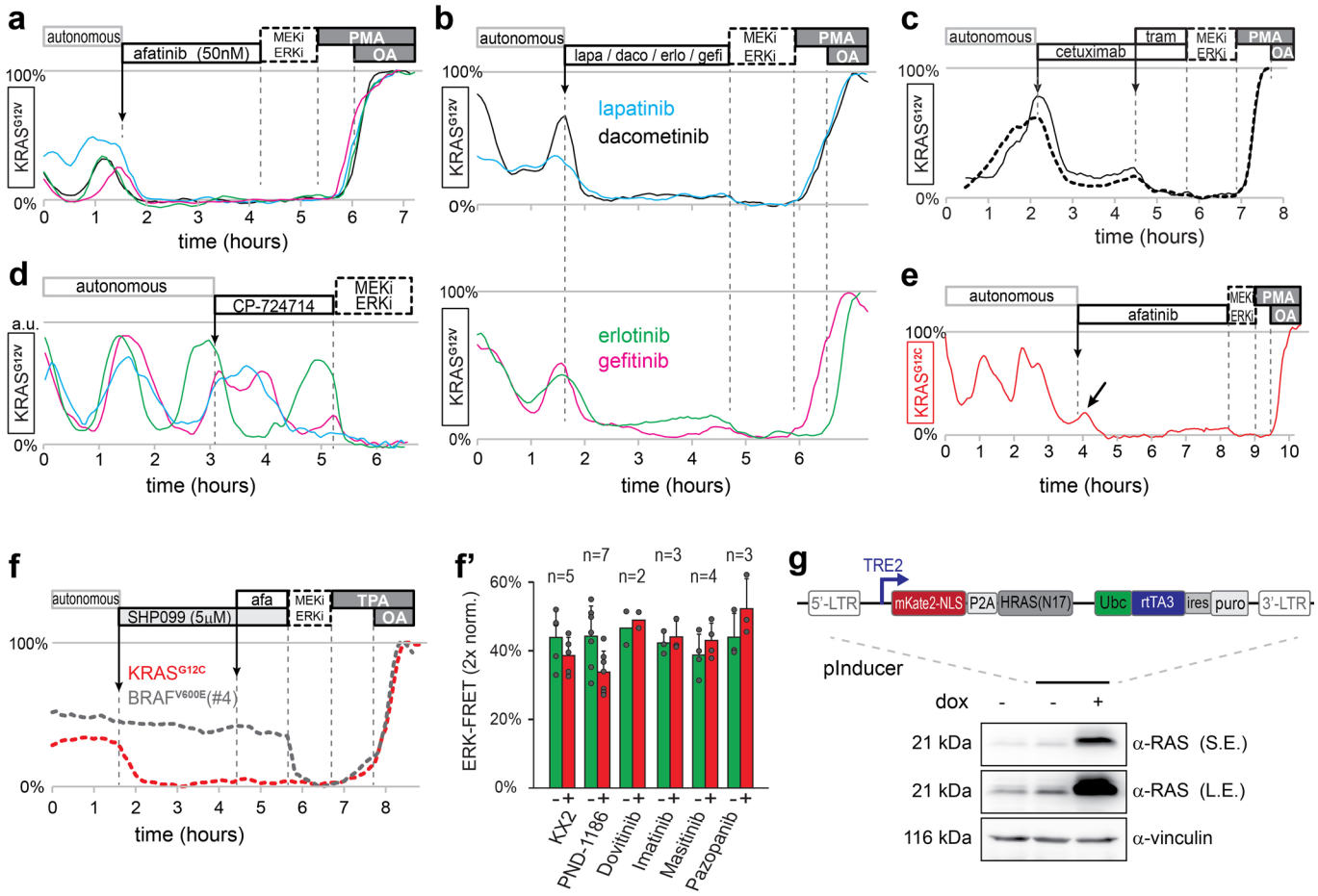

Extended Data Fig. 7 | See next page for caption.

Extended Data Fig. 7 | EGFR plays a central role in generating pulsatile ERK dynamics in PDO-KRAS^{G12V}. a, Fluctuating ERK dynamics in PDO-KRAS^{G12V}, abolished by afatinib at 50nM concentration. Shown traces are representative for 14 single-cell analyses from 3 PDOs. Experiment performed twice. **b**, As **a**, loss of ERK activity oscillations, observed in PDO-KRAS^{G12V} upon administration of pan-HER inhibitors lapatinib (1 μM, 21 cells), dacometinib (500 nM, 12 cells), or EGFR-specific inhibitors erlotinib (500 nM, 17 cells) and gefinitib (500 nM, 18 cells). Two independent experiments performed. ~5 organoids per condition. **c**, As **a**, loss of ERK oscillations, observed in PDO-KRAS^{G12V} upon anti-EGFR antibody cetuximab (500ng/ml). Residual ERK activity was sensitive to trametinib (MEKi). Experiment performed once; 30 cells analyzed. **d**, Oscillating ERK dynamics persist in PDO-KRAS^{G12V} despite HER2-inhibitor CP-724714 (5 μM). Three traces representative for 24 single-cell analyses, from one experiment with 4 organoids. **e**, FRET-trace demonstrating that afatinib (200nM) instantly interrupts rising phase of pulsatile ERK (arrow). Representative for >20 observations in various PDO-lines. **f**, Shp2-inhibitor SHP099 (5μM) abrogates autonomous ERK activity in PDO-KRAS^{G12C}, but not BRAF^{V600E}(#4). Shown are representative multi-cellular z-plane analyses. Experiment performed once; 3 organoids. **f'** BRAF^{V600E}(#4) is similarly unresponsive to drugs targeting Src (KX2, 500 nM), FAK (PND-1186, 500 nM) and cKit/ PDGFR/ Bcr-Abl (dovitinib, 100 nM; imatinib, 1.0 μM; masitinib, 100 nM; pazopanib, 250 nM). Shown are 2x-normalized ratios (mean±s.d.). n numbers represent PDOs and are indicated in the graph per group. Experiment performed once. **g**, Adapted pInducer20 for doxycyclin-inducible expression of HRAS^{N17} and P2A-coupled reporter mKate2-NLS (TRE2, Tet-Responsive Element). Western blot demonstrating doxycyclin-mediated induction of HRAS^{N17} expression (general anti-RAS antibody) in BRAF^{V600E}(#3)(EKAREN5+pInducer). S.E., short exposure; L.E., long exposure. Vinculin as loading control. Experiment performed once. **h**, Western blot analyses on indicated PDOs illustrating pan-HER inhibition on components of the linear EGFR-MAPK-pathway. Pharmacological treatments as in Fig. 4e. Experiment performed once.

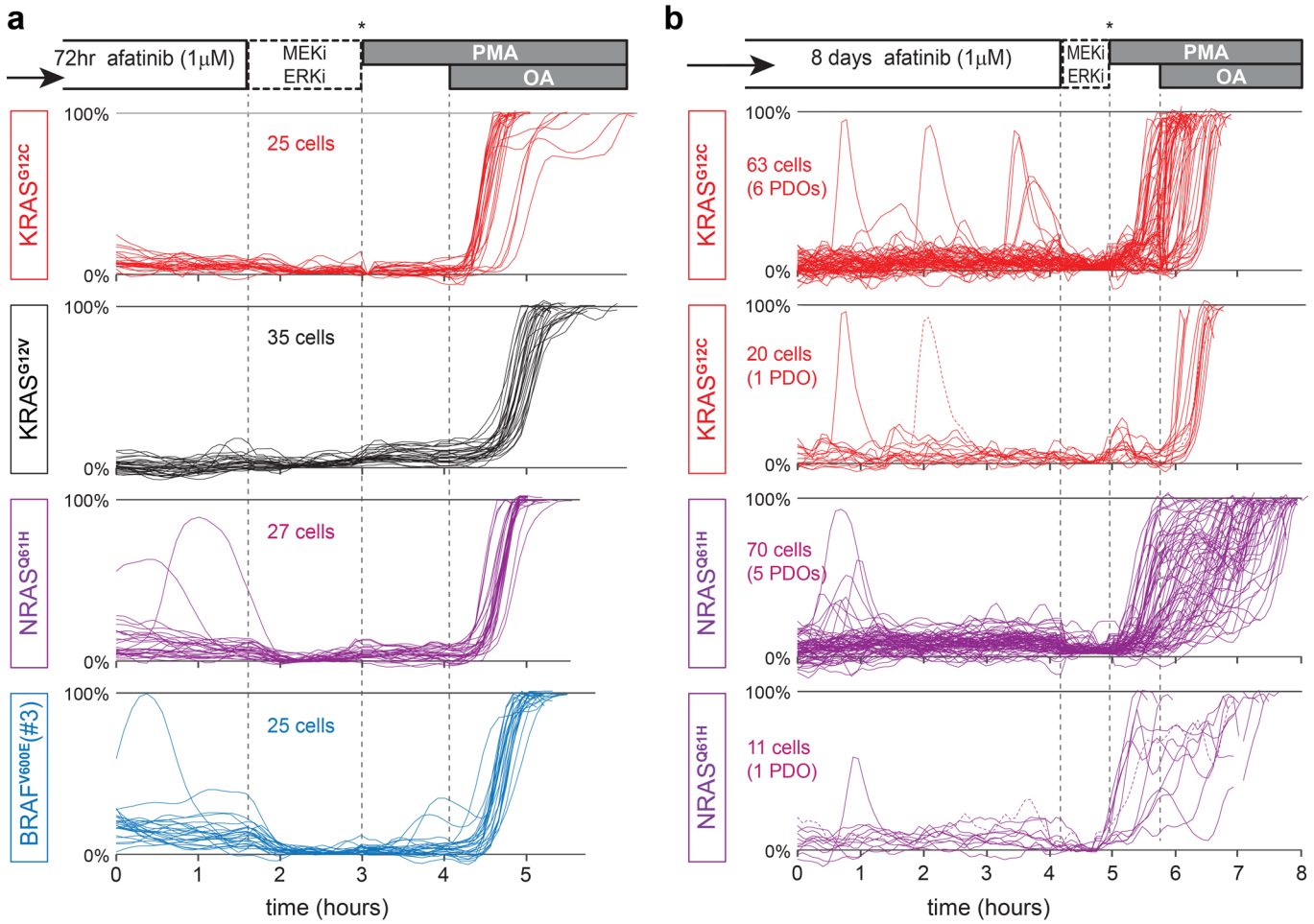

Extended Data Fig. 8 | Single-cell drug response upon long-term exposure to EGFR inhibitors. a, Single-cell analyses from data set presented in Fig. 7b. After 72 hrs afatinib (1 μM), EKAREN5 showed constant, non-oscillatory basal ERK signal. Rare activity spikes in few cells were observed in PDO-NRAS^{Q61H} and BRAF^{V600E}(#3). **b**, Single-cell drug response analysis after 8 days of afatinib treatment (1μM). ERK dynamics in EGFR-inhibited PDO-KRAS^{G12C} (63 cells in 6 organoids) and PDO-NRAS^{Q61H} (70 cells in 5 organoids) are constant, non-oscillatory in nature. Depletion of the continuous oscillatory dynamics unmasked a hidden pattern of (EGFR-independent) rare activity spikes in few cells (one per ~30 hr (19 pulses observed in 571 hours of single-cell signaling evaluation). Never were two pulses observed in one single-cell derivation. Plots show all single cell analyses from multiple organoids or from a single representative organoid. Dotted line: to indicate that the two pulses are from separate cells.

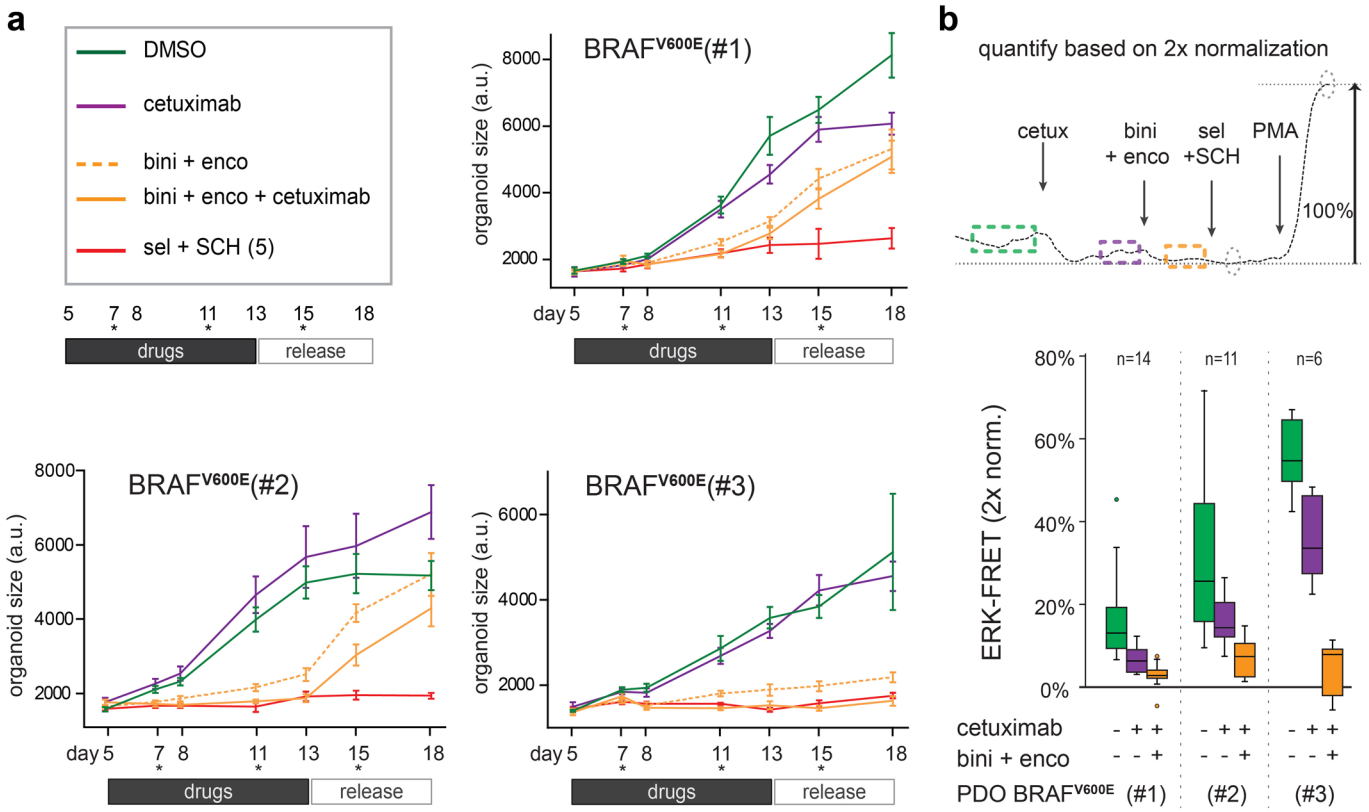

Extended Data Fig. 9 | Examining clinical relevant drug therapy on BRAF mutant PDO. a, Growth assay performed as in Fig. 7c,d, here monitoring the $BRAF^{V600E}$ mutant PDOs #1, #2 and #3 under treatment with drugs from clinical trial by Kopetz et al. (NEJM, 2019[7]). Cetuximab, 1000 ng/ml; binimetinib (MEK-inh), 100 nM; encorafenib (BRAF-inh), 300 nM. Mean number of objects per time point: $BRAF^{V600E}$(#1), n=84; $BRAF^{V600E}$(#2), n=62; $BRAF^{V600E}$(#3), n=78. For the exact n-numbers of all presented points, see Source Data file. Data are represented as mean size ± s.e.m. Growth medium was supplemented with 200x reduced EGF concentration (0.25 ng/ml) to minimize competition between cetuximab and EGF ligand. Experiment performed once. **b**, In same PDO lines, ERK responses were recorded using EKAREN5-FRET. Data are represented as mean value ± s.d. Quantification scheme based on double calibrated multi-cellular z-plane analyses (n numbers represent PDOs and are indicated in the graph for each group). ERK levels were maximally reduced in presence of triple combination. Box-and-whisker plots: boxes represent quartile 2 and 3, horizontal line represents median, whiskers represent minimum and maximum within 1,5x interquartile range. Dots are outliers.

nature research

Corresponding author(s): Hugo J.G. Snippert

Last updated by author(s): February 19, 2021

Reporting Summary

Nature Research wishes to improve the reproducibility of the work that we publish. This form provides structure for consistency and transparency in reporting. For further information on Nature Research policies, see Authors & Referees and the Editorial Policy Checklist.

Statistics

For all statistical analyses, confirm that the following items are present in the figure legend, table legend, main text, or Methods section.

n/a	Confirmed	
☐	☒	The exact sample size (*n*) for each experimental group/condition, given as a discrete number and unit of measurement
☐	☒	A statement on whether measurements were taken from distinct samples or whether the same sample was measured repeatedly
☐	☒	The statistical test(s) used AND whether they are one- or two-sided *Only common tests should be described solely by name; describe more complex techniques in the Methods section.*
☒	☐	A description of all covariates tested
☒	☐	A description of any assumptions or corrections, such as tests of normality and adjustment for multiple comparisons
☐	☒	A full description of the statistical parameters including central tendency (e.g. means) or other basic estimates (e.g. regression coefficient) AND variation (e.g. standard deviation) or associated estimates of uncertainty (e.g. confidence intervals)
☐	☒	For null hypothesis testing, the test statistic (e.g. *F*, *t*, *r*) with confidence intervals, effect sizes, degrees of freedom and *P* value noted *Give P values as exact values whenever suitable.*
☒	☐	For Bayesian analysis, information on the choice of priors and Markov chain Monte Carlo settings
☒	☐	For hierarchical and complex designs, identification of the appropriate level for tests and full reporting of outcomes
☒	☐	Estimates of effect sizes (e.g. Cohen's *d*, Pearson's *r*), indicating how they were calculated

Our web collection on statistics for biologists contains articles on many of the points above.

Software and code

Policy information about availability of computer code

Data collection	FRET imaging was performed on an SP8X Leica laser scanning confocal microscope, equipped with Argon laser and white-light laser, using proprietary software preloaded on the machine for acquisition (Leica LAS X).
Data analysis	All FRET data were analyzed post-acquisition using our own custom-made software, written in the freely available Imagej/Fiji code (ijm-format) (version 1.51n). The various analytical tools for the various types of microscopical acquisitions were all combined in this single analysis script. Design of analytical procedures is extensively described in the Methods Section. The custom-made script can be made available upon request by the corresponding author. Sole exception was the cell-by-cell analysis in large EKAREN5-expressing organoids, presented in Extended data figure 5. Here, segmentation and object-specific Turquoise2 and YPet intensity determinations were performed in Imaris Software (version 9.2). Microsoft excel (version 2019).

For manuscripts utilizing custom algorithms or software that are central to the research but not yet described in published literature, software must be made available to editors/reviewers. We strongly encourage code deposition in a community repository (e.g. GitHub). See the Nature Research guidelines for submitting code & software for further information.

Data

Policy information about availability of data

All manuscripts must include a data availability statement. This statement should provide the following information, where applicable:

- Accession codes, unique identifiers, or web links for publicly available datasets
- A list of figures that have associated raw data
- A description of any restrictions on data availability

All raw FRET data is made available in accompanying source data files. Plasmids generated in this study are available on request and will be deposited on Addgene. All other data supporting the findings of this study are available from the corresponding author on reasonable request.

Field-specific reporting

Please select the one below that is the best fit for your research. If you are not sure, read the appropriate sections before making your selection.

☒ Life sciences ☐ Behavioural & social sciences ☐ Ecological, evolutionary & environmental sciences

For a reference copy of the document with all sections, see nature.com/documents/nr-reporting-summary-flat.pdf

Life sciences study design

All studies must disclose on these points even when the disclosure is negative.

Sample size	No sample-size calculation was performed. Organoid experiments were performed on a panel of 10 patient-derived CRC lines, consisting of at least >3 RAS-mutants, >3 BRAF mutants and 2 lines with normal (WT) MAPK pathway (maximum number we could reasonably obtain). Single-cell experiments for sensor characterizations were performed on maximally feasible numbers. Results obtained were highly significant and consistent and did not require additional experiments. Sample sizes are indicated throughout manuscript and in accompanying source data files.
Data exclusions	Single-cell analyses from CRC organoids were excluded when clearly suffering from geometry-related artefact (e.g. movement in depth or incorrect confocal slicing)
Replication	Our main finding, namely that EGFR acts as a massive amplifier of (oncogenic) MAPK pathway signaling, was observed in 9 out of 10 patient-derived organoid lines (the outlier HUB096 is extensively described). Furthermore, per PDO, these observations were consistent over months of experimentation (>10 experiments per PDO line, and >5PDOs per experiment per line). The number of times each experiments was replicated are indicated in each figure legend and accompanying source data files.
Randomization	Organoids to be analyzed were chosen randomly.
Blinding	Data acquisition was not performed blindly, due to PDO line and sensor specific phenotypes and/or characteristics.

Reporting for specific materials, systems and methods

We require information from authors about some types of materials, experimental systems and methods used in many studies. Here, indicate whether each material, system or method listed is relevant to your study. If you are not sure if a list item applies to your research, read the appropriate section before selecting a response.

Materials & experimental systems

n/a	Involved in the study
☐	☒ Antibodies
☐	☒ Eukaryotic cell lines
☒	☐ Palaeontology
☒	☐ Animals and other organisms
☐	☒ Human research participants
☒	☐ Clinical data

Methods

n/a	Involved in the study
☒	☐ ChIP-seq
☒	☐ Flow cytometry
☒	☐ MRI-based neuroimaging

Antibodies

Antibodies used	Antibodies used: a) pEGFR(Y1068) (Cell Signaling, #2234), dilution : 1:1000 b) EGFR (Cell Signaling, #4267), dilution : 1:1000 c) Ras (BD Biosciences, RRID:AB_397425), dilution : 1:1000 d) pMEK1/2 (Ser217/221) (Cell Signaling, #9121, RRID:AB_331648), dilution : 1:1000 e) MEK1/2 (Cell Signaling, #9122, RRID:AB_823567), dilution : 1:1000

f) ERK1/2 (Cell Signaling, #4695, RRID:AB_390779), dilution : 1:1000
g) pERK1/2(Thr202/Tyr204) (Cell Signaling, #4370, RRID:AB_2315112), dilution : 1:1000
h) Vinculin (Sigma-Aldrich, V9131, RRID:AB_477629), dilution : 1:1000

Validation

Antibodies are validated for the used purpose by the vendor. All antibodies are used in previous studies, which references can be found on the supplier website.

Eukaryotic cell lines

Policy information about cell lines

Cell line source(s)

5 out of 10 studied organoid lines are derived from human colorectal cancer tissues, and were previously described by van de Wetering et al., Cell, 2015. (being p6T (KRasG12C), p9T (KRasG12V), p25T (NRasQ61H), p19bT (BRafV600E(#2)) and p18T (WT #1)).
1 out of 10 studied organoid lines are derived from human colorectal cancer tissues, and were previously described by Roerink et al., Nature 2018. (being p1T4 (BRafV600E(#1)).
4 out of 10 were obtained from the HUB biobank (Foundation Hubrecht Organoid Technology, Utrecht, the Netherlands) and can be acquired from the HUB. (Being HUB-02-B2-040 (BRAFV600E(#3)), HUB-02-B2-096 (BRAFV600E (#4)), HUB-02-B2-113 (KRasG12D) and HUB-02-B2-074 (WT(#2)).
All organoid lines, official names and/or catalogue numbers are extensively described in suppl. table 1.

RASless MEFs were obtained via the Voest lab (NKI). RASless MEFs identify was confirmed by PCR and Sanger sequencing of reconstituted RAS/RAF variant. HEK293 and HeLa cell lines are commonly used within our department and were identified based on unique morphological phenotypes.

Authentication

PCR amplification and Sanger sequencing was used to detect and confirm presence of known point mutations that are unique per patient organoid sample.
PCR amplification and Sanger sequencing was used of reconstituted RAS/BRAF cDNA to confirm identity of RASless MEFs.
HEK293 and HeLa cells were identified based on known morphological characteristics.

Mycoplasma contamination

Samples have repeatedly been tested negative for Mycoplasma

Commonly misidentified lines
(See ICLAC register)

No commonly misidentified cell lines were used

Human research participants

Policy information about studies involving human research participants

Population characteristics

Human colorectal cancer tissue (treatment naive) was obtained from patients (age and gender not disclosed) from the UMC Utrecht and processed by the HUB (Foundation Hubrecht Organoid Technology, Utrecht, the Netherlands) to generate a colorectal cancer organoid biobank. The study has been performed according to the guidelines of the European Network of Research Ethics Committees (EUREC) following European, national, and local law.

Recruitment

Available tissue from patients with informed consent were collected without any bias in selection of the participants. Organoid lines were selected from the available HUB biobank based on the presence/absence of oncogenic RAS or BRAF mutations.

Ethics oversight

Dutch Ethical Medical Council (UMC Utrecht).

Note that full information on the approval of the study protocol must also be provided in the manuscript.